



RESEARCH ARTICLE SUMMARY

CELL BIOLOGY

The midnolin-proteasome pathway catches proteins for ubiquitination-independent degradation

Xin Gu[†], Christopher Nardone[†], Nolan Kamitaki, Aoyue Mao, Stephen J. Elledge^{*}, Michael E. Greenberg^{*}

INTRODUCTION: In mammals, the transcriptional response to growth factor, neuronal, and immune stimuli is mediated by a group of genes called immediate-early genes (IEGs), which encode transcription factors of the *Fos*, *EGR*, and *NR4A* families. IEG proteins are activated stereotypically in virtually all mammalian cells but promote the transcription of late-response genes (LRGs) that are cell-type specific and crucial for the appropriate response to the initial stimulus. The physiological importance of IEGs is underscored by the fact that misregulation of their expression can lead to cancer, immune deficiencies, and neurological disorders. The IEG mRNAs accumulate within minutes after the initial stimulus and, once translated, their proteins are rapidly degraded to allow for a transient burst of protein expression. Although the mechanisms that regulate IEG transcription are well characterized, how IEG proteins are swiftly targeted for destruction has remained mysterious for many years.

RATIONALE: Eukaryotic cells rely on a macromolecular protease called the proteasome that

canonically degrades proteins marked with ubiquitin. It has been suggested that the *Fos* family is targeted to the proteasome by both ubiquitination-dependent and -independent mechanisms, but the molecular events that orchestrate these processes have remained elusive. We hypothesized that there exists a cellular pathway dedicated to the rapid destruction of c-Fos and other IEG proteins. By harnessing the power of forward genetic screens, we sought to identify the machinery that controls the degradation of these proteins.

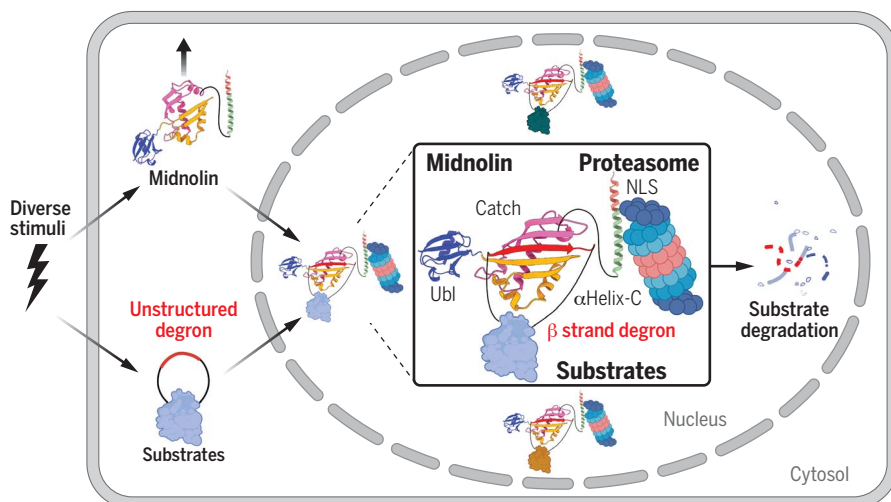
RESULTS: We performed genome-wide CRISPR-Cas9 screens to search for genes that regulate the stability of IEG proteins. We found that midnolin, a largely uncharacterized protein in mammals, promoted the proteasomal destruction of IEG proteins from structurally distinct families including c-Fos, FosB, EGRI, and NR4A1. These results prompted us to search for additional midnolin targets. We used the global protein stability (GPS) assay with a human open reading frame library (ORFeome) to assess changes in protein stability for ~12,000 human proteins simultaneously. In addition to

IEG proteins, midnolin promoted the degradation of IRF4, NeuroD1, PAX8, GATA1, many other cell-type-specific transcriptional regulators in the nucleus, where midnolin itself resides.

Diverse stimuli that activate IEGs also induced midnolin, and midnolin overexpression was sufficient to cause the destruction of its targets by a mechanism that does not require ubiquitination. Multiple lines of evidence support this ubiquitination-independent mechanism of protein degradation. Midnolin still bound to and promoted the degradation of many targets that had been mutated to lack lysine residues. Moreover, inhibition of the proteasome, but not E1 ubiquitin-activating enzymes, abrogated midnolin function. Additionally, midnolin does not contain RING or HECT domains that are characteristic of E3 ubiquitin ligases or ubiquitin-binding domains found in proteasomal processivity factors such as Rad23.

Instead, midnolin engaged substrates using its “Catch” domain, which was necessary and sufficient to interact with unstructured regions within substrates that have the potential to form a β strand upon binding midnolin. These unstructured regions with the propensity to form a β strand were also necessary and sufficient to bind the Catch domain, thus functioning as a midnolin degron. In addition, midnolin stably associated with the proteasome through a C-terminal α helix and promoted the degradation of Catch-bound targets using its N-terminal ubiquitin-like domain. Thus, midnolin contains three conserved structural domains that function in concert to directly target a large set of nuclear proteins to the proteasome for ubiquitination-independent degradation.

CONCLUSION: Our study suggests that the midnolin-proteasome pathway may represent a general mechanism by which the proteasome bypasses the canonical ubiquitination system to achieve selective degradation of nuclear proteins, many of which are crucial for transcription. Within substrates, midnolin recognizes relatively degenerate amphipathic regions with the potential to form β strands, so the midnolin degron may be a common structural component of numerous proteins. How the midnolin-proteasome pathway is regulated by various cues in diverse cell types to control transcriptional programs will be an important subject of future exploration. ■



The midnolin-proteasome pathway degrades many nuclear proteins independently of ubiquitination.

Midnolin is induced by diverse cues, including growth factors and neuronal stimuli. Within the nucleus, midnolin associates with the proteasome through a C-terminal α helix (α Helix-C) and promotes the degradation of bound substrates using an N-terminal ubiquitin-like domain (Ubl). Midnolin achieves selectivity using its Catch domain, which binds an unstructured region within substrates that can form a β strand. Structures shown are AlphaFold models. Figure was created with BioRender.com. NLS, nuclear localization sequence.

The list of author affiliations is available in the full article online.

^{*}Corresponding author. Email: selledge@genetics.med.harvard.edu (S.J.E.); michael_greenberg@hms.harvard.edu (M.E.G.)

[†]These authors contributed equally to this work.

Cite this article as X. Gu et al., *Science* **381**, eadh5021 (2023). DOI: 10.1126/science.adh5021

S READ THE FULL ARTICLE AT
<https://doi.org/10.1126/science.adh5021>

RESEARCH ARTICLE

CELL BIOLOGY

The midnolin-proteasome pathway catches proteins for ubiquitination-independent degradation

Xin Gu^{1†}, Christopher Nardone^{2,3†}, Nolan Kamitaki^{3,4}, Aoyue Mao^{2,3,5}, Stephen J. Elledge^{2,3*}, Michael E. Greenberg^{1*}

Cells use ubiquitin to mark proteins for proteasomal degradation. Although the proteasome also eliminates proteins that are not ubiquitinated, how this occurs mechanistically is unclear. Here, we found that midnolin promoted the destruction of many nuclear proteins, including transcription factors encoded by the immediate-early genes. Diverse stimuli induced midnolin, and its overexpression was sufficient to cause the degradation of its targets by a mechanism that did not require ubiquitination. Instead, midnolin associated with the proteasome via an α helix, used its Catch domain to bind a region within substrates that can form a β strand, and used a ubiquitin-like domain to promote substrate destruction. Thus, midnolin contains three regions that function in concert to target a large set of nuclear proteins to the proteasome for degradation.

In mammals, extracellular growth factors, cytokines, neurotrophic factors, and neurotransmitters bind their cognate receptors and activate rapid responses by inducing posttranslational modifications of preexisting proteins. More delayed responses are also induced by stimulating gene transcription within the nucleus (1, 2). This transcriptional response occurs in two steps. First, within minutes of the initial stimulus, a set of genes called immediate-early genes (IEGs) is activated. The IEGs encode transcription factors that then trigger a second wave of late-response gene (LRG) expression that mediates the cellular response to the initial stimulus. The IEG response is activated in a stereotypical fashion in virtually every cell type in the body but induces programs of LRG expression that are cell-type specific (3). The plethora of cellular responses regulated by IEGs include the cell cycle reentry of quiescent fibroblasts during wound healing; the activation of immune cells in response to cytokines and bacterial and viral infections; and the adaptive responses of neurons to neurotransmitters during learning and memory (3).

The IEG family encodes transcription factors such as *Fos*, *Egr*, and *Nr4a* that are rapidly and transiently induced in response to a wide range of extracellular stimuli (4). The IEG mRNAs accumulate to a high level, and once these mRNAs

are translated, the IEG proteins undergo rapid decay (5). Thus, the protein stability of the IEG program is tightly controlled to allow for a relatively brief burst of protein expression that is crucial for appropriate cellular responses to various stimuli. Misregulation of the signaling networks that control IEG expression can lead to cancer, immune deficiencies, and neurological disorders (3).

Although the mechanisms that regulate IEG transcription are well characterized, it is unclear how IEG proteins are degraded. In many cases, conjugation of ubiquitin onto substrate proteins occurs as a prelude to their destruction by the proteasome. *c-Fos* and *FosB* have been reported to be targeted to the proteasome by both ubiquitination-dependent and -independent mechanisms, but the molecular events that orchestrate these processes are unknown (6, 7).

Genetic screens reveal midnolin as a regulator of IEG protein degradation

To investigate the mechanism of IEG protein degradation, we first used the global protein stability (GPS) reporter system to assay IEG protein stability (8). GPS allows for the stable expression of DsRed as an internal control and a green fluorescent protein (GFP)-tagged protein from the same bicistronic mRNA. Therefore, the ratio of GFP/DsRed analyzed by flow cytometry provides a measure of the relative stability of the GFP-fused protein. To identify regulators of IEG protein stability, we generated human embryonic kidney (HEK)-293T cell lines stably expressing the GPS reporter for *EGR1* or *FosB* and performed genome-wide CRISPR-Cas9 screens to search for genes whose disruption stabilized *EGR1* or *FosB* (Fig. 1A). The comparison of *EGR1* and *FosB* allowed us to investigate whether IEGs from different families are degraded by the same or different mecha-

nisms. The top hit from both screens was *MIDN*, a gene that in mammals encodes a largely uncharacterized protein named midnolin (Fig. 1, B and C, and data S1).

To validate our CRISPR-Cas9 screening results, we generated *MIDN* clonal knockout (KO) HEK-293T cells stably expressing the GPS reporter for *EGR1* or *FosB* and assessed the effect of *MIDN* disruption and overexpression on the stability of *EGR1* or *FosB*. Consistent with the screening results, loss of midnolin increased the stability of both *EGR1* and *FosB* (Fig. 1, D and E). We tested additional IEG proteins, and midnolin overexpression was sufficient to decrease the levels of *EGR1*, *FosB*, *c-Fos*, and *NR4A1* (Fig. 1, D and E, and fig. S1, A and B) but not several other transcription factors, including *ATF2*, *CREB3*, and *CREB5* (fig. S1C). These findings raised an interesting possibility that three distinct families of IEG proteins may be targeted for degradation by the same protein: midnolin.

Midnolin is induced and promotes the degradation of several IEG proteins in physiological settings

To investigate the requirement of midnolin for the degradation of IEG proteins in physiologically relevant settings, we mutated *MIDN* using CRISPR-Cas9 to generate a population-level KO of NIH/3T3 fibroblasts, a well-characterized cell line for studying IEG inducibility during cell cycle reentry. Serum deprivation synchronizes NIH/3T3 cells in the G_0 phase of the cell cycle, and IEGs are rapidly and transiently transcribed within minutes after serum addition to these cells (9). This transient induction of IEG transcription is followed by an increase in the levels of IEG proteins that then quickly return to their basal levels. In *MIDN* KO cells, IEG protein levels remained high for several hours longer than in control cells, suggesting that the degradation of *EGR1*, *NR4A1*, *FosB*, and *c-Fos* was attenuated in the absence of midnolin (Fig. 2A). By contrast, stable overexpression of midnolin led to a decrease in the levels of these IEG proteins (Fig. 2B).

In addition to their importance during cell cycle reentry, IEGs mediate adaptive responses in neurons. In response to sensory stimuli, if enough glutamate is released at excitatory synapses in the brain to generate an action potential in the postsynaptic neuron, the depolarization of this neuron results in an influx of calcium that triggers the induction of IEGs (3). This membrane depolarization induction of IEGs also occurs in cultured mouse neurons within minutes of exposure to elevated levels of KCl (10). To determine whether midnolin regulates IEG protein levels in this paradigm, embryonic mouse cortical neurons were cultured and infected with lentivirus to generate population-level *MIDN* KO or midnolin-overexpressing cells. When exposed to elevated levels of KCl, IEG protein

¹Department of Neurobiology, Harvard Medical School, Boston, MA 02115, USA. ²Division of Genetics, Department of Medicine, Howard Hughes Medical Institute, Brigham and Women's Hospital, Boston, MA 02115, USA. ³Department of Genetics, Harvard Medical School, Boston, MA 02115, USA. ⁴Department of Biomedical Informatics, Harvard Medical School, Boston, MA 02115, USA. ⁵Department of Molecular and Cellular Biology, Harvard University, Cambridge, MA 02138, USA.

*Corresponding author. Email: selledge@genetics.med.harvard.edu (S.J.E.); michael_greenberg@hms.harvard.edu (M.E.G.)

†These authors contributed equally to this work.

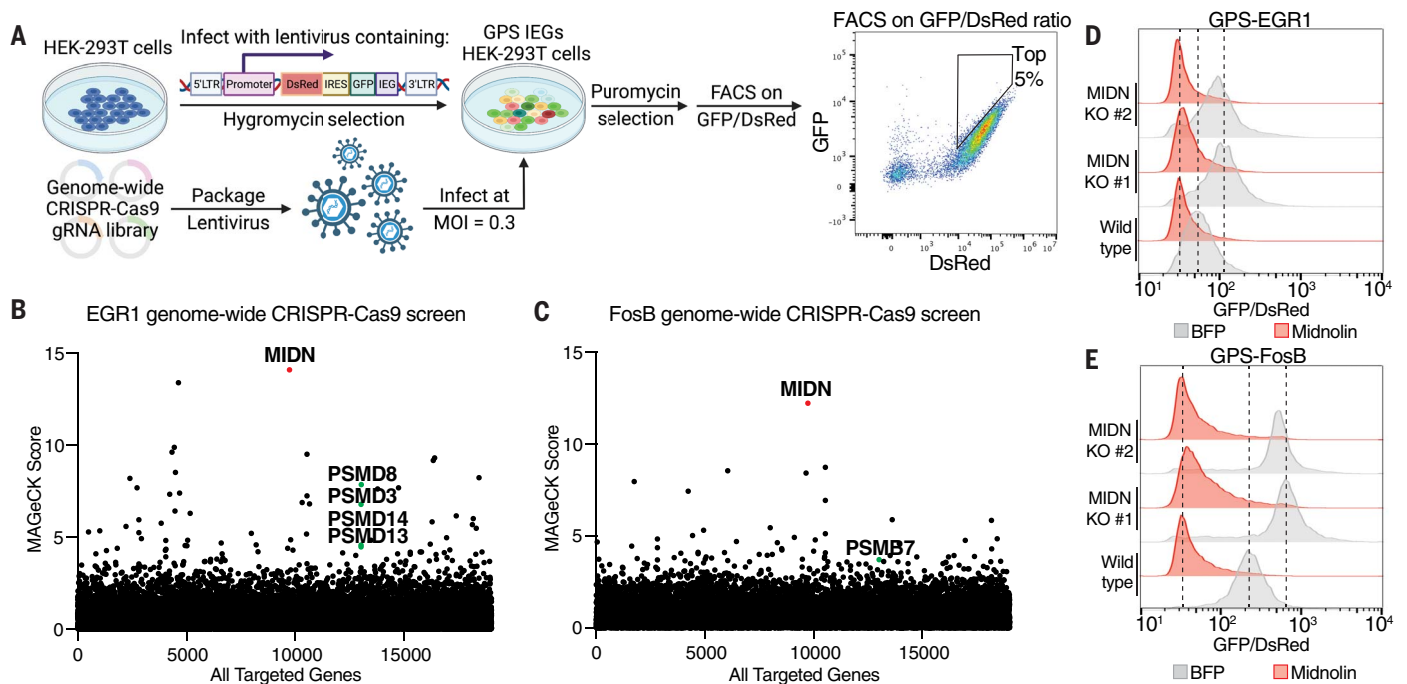


Fig. 1. Genetic screens reveal midnolin as a regulator of IEG protein degradation. (A) Schematic showing the FACS-based genome-wide CRISPR-Cas9 screens using the GPS reporter of IEG proteins in HEK-293T cells (figure created with BioRender.com). (B and C) Results of the genetic screens revealed *MIDN* as the top hit for negatively regulating the stability of both EGR1 and FosB. The proteasomal components showed a weaker enrichment, likely due to their essentiality. The MAGeCK score represents the negative log₁₀ of the

“pos|score” value generated from MAGeCK (62). (D and E) Losing midnolin stabilized, whereas overexpressing midnolin destabilized, EGR1 and FosB. GPS EGR1 or FosB reporters were stably expressed in wild-type and two independent *MIDN* KO HEK-293T single cell clones. Vectors expressing BFP control alone (gray) or midnolin and BFP from a EF1 α promoter (red) were transiently reintroduced by transfection before analyzing the GFP/DsRed ratio by flow cytometry.

expression was increased in *MIDN* KO neurons but decreased in the midnolin-overexpressing neurons (Fig. 2, C and D). By contrast, IEG mRNA expression was largely unchanged by midnolin overexpression (fig. S1D), which is consistent with midnolin affecting the stability of IEG proteins but not their mRNA transcripts.

KCl treatment of primary cortical neurons induced *MIDN* mRNA levels with kinetics similar to that of IEGs (Fig. 2E). In a previous RNA-sequencing dataset, *MIDN* was found to be induced upon light stimulation of the visual cortex in vivo (fig. S1E) (11). Midnolin was also induced upon serum restimulation of NIH/3T3 cells (Fig. 2F) with kinetics similar to that of IEGs (12). These stimulus-dependent increases in midnolin expression may be involved in the rapid degradation of IEG proteins. Thus, midnolin is induced by various stimuli and promotes the degradation of IEG proteins in physiologically relevant settings, potentially through a feedback mechanism.

Midnolin can promote the degradation of numerous transcriptional regulators

To determine the extent to which midnolin regulates other cellular proteins beyond IEGs, we performed a screen to identify additional midnolin targets. The screen used a previously described GPS ORFeome library, which contains

~12,000 barcoded human open reading frames (ORFs) tagged with GFP in the GPS reporter system (13). The GPS ORFeome library was stably introduced into *MIDN* KO HEK-293T cells, and plasmids expressing either a control blue fluorescent protein (BFP) or midnolin together with BFP were transiently transfected into cells to yield two cell libraries, one lacking midnolin and the other overexpressing midnolin. Because the GPS system overexpresses proteins and endogenous midnolin levels are low, we overproduced midnolin to gain sensitivity in this setting. The cells in each library were then partitioned into six populations on the basis of their GFP/DsRed ratios by fluorescence-activated cell sorting (FACS). The barcodes present in each population were then sequenced to determine the change in their distribution within the cell populations upon midnolin overexpression. If midnolin promoted the destruction of a given barcoded GFP-fusion protein, then the distribution of the barcode would shift to a cell population with a lower GFP/DsRed ratio in the midnolin-overexpressing library (Fig. 3A). This screen yielded our previously characterized targets of midnolin, including FosB and c-Fos, along with CBX4 (Pc in flies), which was previously shown to be regulated by the *Drosophila melanogaster* ortholog of midnolin, Stuxnet (14) (Fig. 3B). Midnolin overexpression also led to a

robust reduction in the GFP/DsRed ratios of many proteins, consistent with a decrease in protein stability (data S2). Most of the proteins regulated by midnolin overexpression were nuclear proteins that regulate transcription (Fig. 3C), such as the lineage-specific transcription factors IRF4, NeuroD1, PAX8, and GATA1.

To validate the findings from the GPS ORFeome screen, midnolin was overexpressed in *MIDN* KO HEK-293T cells stably expressing individual GPS reporters for the identified proteins. Midnolin overexpression was sufficient to reduce the GFP/DsRed ratios of these proteins, consistent with a decrease in their stability (Fig. 3D and fig. S2A). The endogenous levels of various proteins identified in the screen were also substantially reduced in HEK-293T cells that expressed a doxycycline-induced midnolin (Fig. 3E). Among the lineage-specific transcription factors that are not expressed in HEK-293T cells, interferon regulatory factor 4 (IRF4) is essential for the function and homeostasis of mature B and T cell lymphocytes (15, 16). To test the ability of midnolin to promote the destruction of endogenous IRF4, we generated Ramos B cell lines with population-level KO or overexpression of midnolin. In these cell lines, the steady-state levels of IRF4 were markedly increased in the *MIDN* KO cells and decreased in the midnolin-overexpressed cells (Fig. 3F). Thus,

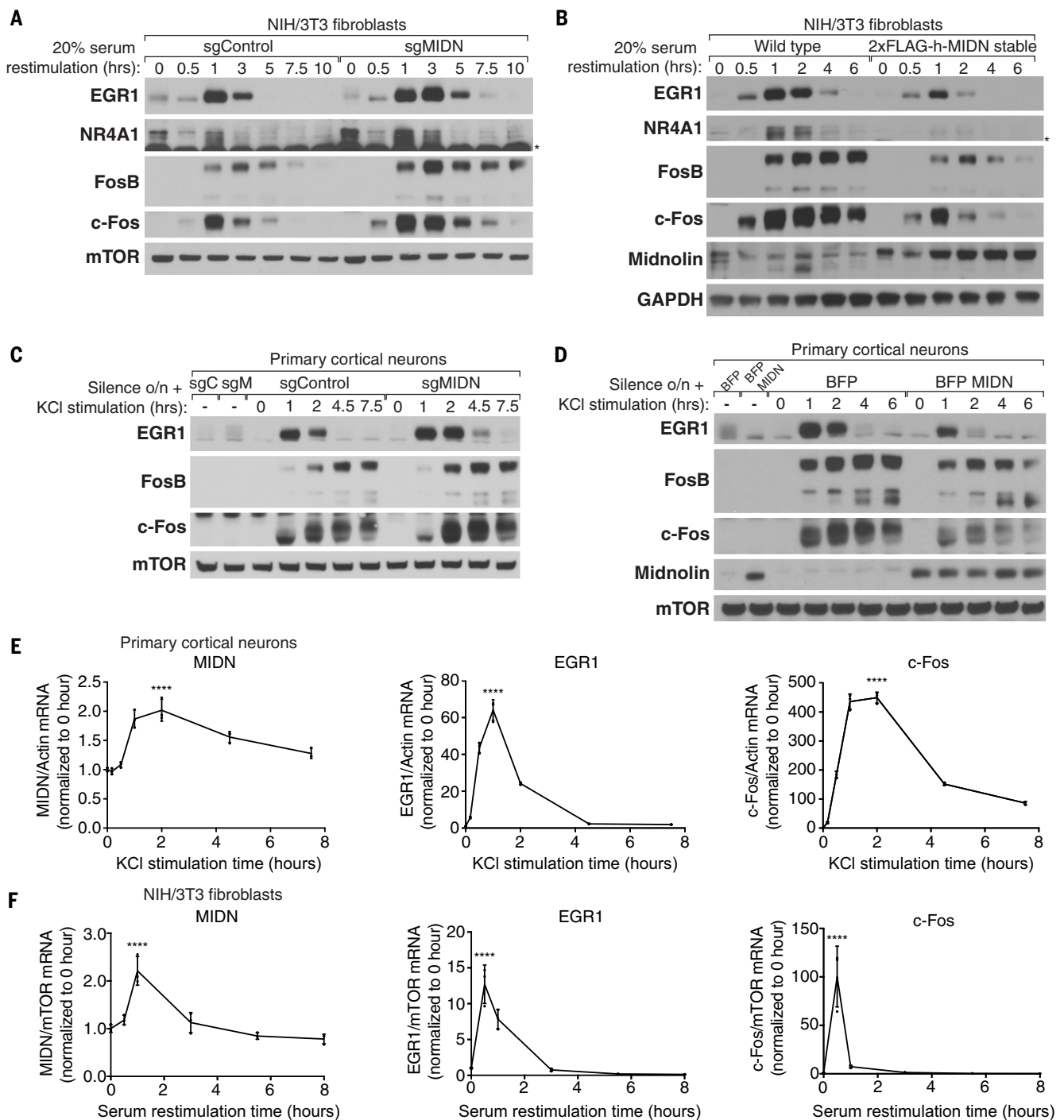


Fig. 2. Midnolin is induced and promotes the degradation of several IEG proteins in physiological settings.

(A) Loss of midnolin increased the expression of IEG proteins in NIH/3T3 cells. Immunoblotting was performed from NIH/3T3 cells stably expressing Cas9 and control or *MIDN* targeting sgRNAs. This population-level mutagenesis of *MIDN* may show lower penetrance relative to an isogenic mutant because the KO efficiency is dependent on the efficacy of the sgRNA. The cells were starved of serum overnight before serum restimulation for the indicated time points. Asterisks mark nonspecific cross-reactive proteins. **(B)** Overexpressing midnolin decreased the expression of IEG proteins in NIH/3T3 cells. Same assay as in (A) but in NIH/3T3 cells stably overexpressing an N-terminally 2xFLAG tagged human midnolin using a CMV promoter. **(C)** Loss of midnolin increased the expression of IEG proteins in primary cortical neurons. Neurons were isolated from E16.5 mouse brains and cultured in a dish. On day 3

after isolation, the neurons were infected with lentivirus encoding Cas9 with control or *MIDN* targeting sgRNAs. Immunoblotting was performed on day 11 after dissection from neurons that were silenced overnight with TTX (a sodium channel blocker) and D-AP5 (an NMDA receptor antagonist) and stimulated with KCl for the indicated time points to induce depolarization. **(D)** Overexpressing midnolin decreased the expression of IEG proteins in primary cortical neurons. Similar assay as in (C) but using lentivirus to overexpress a BFP control or human midnolin coexpressing BFP using an EF1 α promoter. **(E and F)** qPCR analysis for mRNA levels of the indicated genes from primary mouse cortical neurons that were KCl stimulated (E) or from NIH/3T3 cells that were serum restimulated (F) for the indicated time points. Error bars indicate SD from three biological replicates. Data were analyzed using an ordinary one-way ANOVA followed by Tukey's multiple-comparisons test; **** $P < 0.0001$.

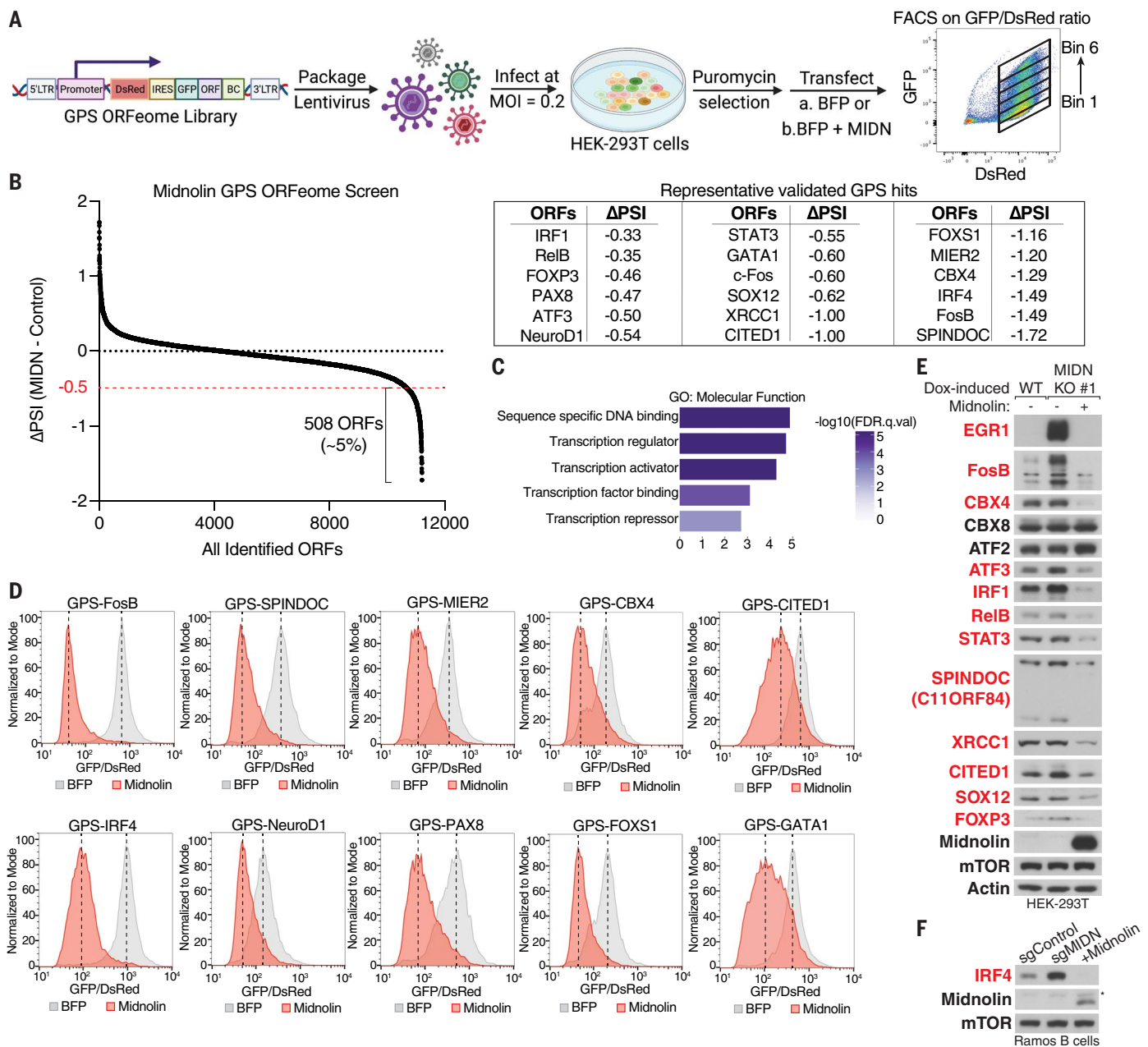


Fig. 3. Midnolin can promote the degradation of numerous transcriptional regulators.

(A) Schematic showing the midnolin GPS ORFeome screen. The GPS ORFeome library (~12,000 barcoded human ORFs tagged to GFP) was introduced into *MIDN* KO HEK-293T, and the library-expressing cells were transfected with BFP control or midnolin coexpressing BFP before FACS sorting the library into populations based on the GFP/DsRed ratio (figure created with BioRender.com). (B) Analysis of the GPS ORFeome screen showing the change in protein stability (Δ PSI) between midnolin and BFP, which was calculated based on the change in read distribution of the barcoded ORFs. Approximately 5% of the library showed significant destabilization with Δ PSI values ≤ -0.5 . Several validated hits from the screen are shown in the boxed table. (C) GSEA based on the GPS ORFeome screen for molecular function. (D) Validation of screen hits

indicates their potent regulation by midnolin. GPS reporters for the indicated genes were stably expressed in *MIDN* KO HEK-293T cells, and a control BFP or midnolin coexpressing BFP was transiently transfected before analyzing the GFP/DsRed ratio by flow cytometry. (E) Endogenous proteins of numerous screen hits are regulated by midnolin. Immunoblotting was performed from wild-type, *MIDN* KO, and *MIDN* KO HEK-293T cells in which midnolin expression was stably induced with doxycycline (100 ng/ml) for 2 days using a TRE promoter. Shown are putative midnolin targets (red) based on the GPS ORFeome screen and negative controls (black). (F) Validation of midnolin-mediated degradation of endogenous IRF4 in Ramos B cells. Immunoblotting was performed from Ramos B cells expressing Cas9, control or *MIDN* targeting sgRNAs, or stably overexpressing midnolin using an EF1 α promoter.

through gain-of-function screening, we uncovered many potential targets of midnolin that have important tissue or cell type-specific functions in regulating gene expression.

Midnolin associates both with its substrates and the 26S proteasome

To begin to determine how midnolin promotes the degradation of a large diverse set of pro-

teins, we generated a HEK-293T cell line in which endogenous midnolin was tagged at its N terminus with 3xHA to facilitate immunoprecipitation. We found by mass spectrometry

that endogenous midnolin coimmunoprecipitated essentially all proteasomal subunits of the 19S regulatory particle and the 20S proteolytic core particle (Fig. 4A and data S3). These proteasomal subunits were the most abundant proteins detected by mass spectrometry. Also, there were no proteins aside from the proteasomal proteins that were both coimmunoprecipitated by midnolin and scored in our genome-wide CRISPR-Cas9 screens (data S3 and Fig. 1, A to C). These results suggested that midnolin likely interacts directly with the proteasome. In addition, by mining the BioPlex protein-protein interaction dataset (17), we found that several IEG proteins, including EGRI, FosB, and NR4A1, as well as a proteasomal component, PSMD2, coimmunoprecipitated endogenous midnolin in HEK-293T cells (fig. S3A).

To confirm the mass spectrometry findings, we treated HEK-293T cells expressing 3xHA-tagged midnolin with MG132 to prevent substrate degradation or with phorbol 12-myristate 13-acetate (PMA), a protein kinase C agonist, to induce the transcription of IEGs (18). Endogenous midnolin interacted with c-Fos, FosB, EGRI, and NR4A1, as well as the proteasome, as indicated by PSMD2 and PSMA2, components of the 19S and 20S proteasome, respectively (Fig. 4B). Like serum-stimulated fibroblasts and KCl-treated neurons, exposure of HEK-293T cells to PMA led to an increase in the level of the midnolin protein (Fig. 4B). Thus, midnolin interacts with the proteasome to promote the degradation of midnolin-bound proteins.

Midnolin promotes ubiquitination-independent degradation of bound substrates

We next investigated whether midnolin targets its substrates for destruction by a ubiquitination- and proteasome-dependent mechanism. Individual GPS reporters of midnolin substrates were stably expressed in *MIDN* KO HEK-293T cells, which were transfected with BFP control or midnolin coexpressing BFP. These reporter cells were then treated for 6 hours with the proteasome inhibitor MG132 or TAK-243, a potent inhibitor of the E1 ubiquitin-activating enzymes UBA6 and UAE that inhibits protein ubiquitination globally (19). Although the proteasome inhibitor MG132 strongly reduced the midnolin-mediated degradation of these midnolin substrates, the ubiquitin E1 inhibitor TAK-243 did not disrupt midnolin function (fig. S3B). By contrast, both MG132 and TAK-243 promoted stabilization of c-Myc, which does not appear to be a midnolin substrate (fig. S3B). Furthermore, when we treated HEK-293T cells expressing 3xHA-tagged midnolin with MG132 or TAK-243 for 6 hours, we found that the proteasome inhibitor MG132 led to a potent increase in the expression of the midnolin protein, but the E1 inhibitor TAK-243 caused a slight decrease in the level of midnolin. Conversely, the level of c-Myc and p27, two transcriptional regulators

that are known to be targeted for proteasomal degradation in a ubiquitination-dependent manner, increased upon exposure to TAK-243 or MG132 (Fig. 4C) (20–22). Thus, midnolin does not appear to require ubiquitination for its own turnover by the proteasome.

To further test the requirement of ubiquitination for midnolin-mediated degradation, potential ubiquitination sites were mutated in several midnolin substrates. Because canonical ubiquitination occurs on lysine residues, all lysine residues within these substrates were mutagenized to arginine to block lysine-dependent ubiquitination (23–25). Wild-type and K-to-R mutant substrates, such as EGRI, FosB, c-Fos, NR4A1, NeuroD1, and IRF4, interacted with endogenous midnolin to a similar extent (Fig. 4D). When stably expressed in *MIDN* KO HEK-293T cells, both wild-type and K-to-R mutant substrates were efficiently degraded upon doxycycline-induced midnolin overexpression (Fig. 4E), indicating that lysine residues were not required for midnolin-dependent substrate destruction. Thus, it seems that midnolin directly associates with the proteasome and promotes the degradation of many transcriptional regulators without requiring their ubiquitination.

Midnolin contains three domains that function in concert to promote proteasomal degradation of bound substrates

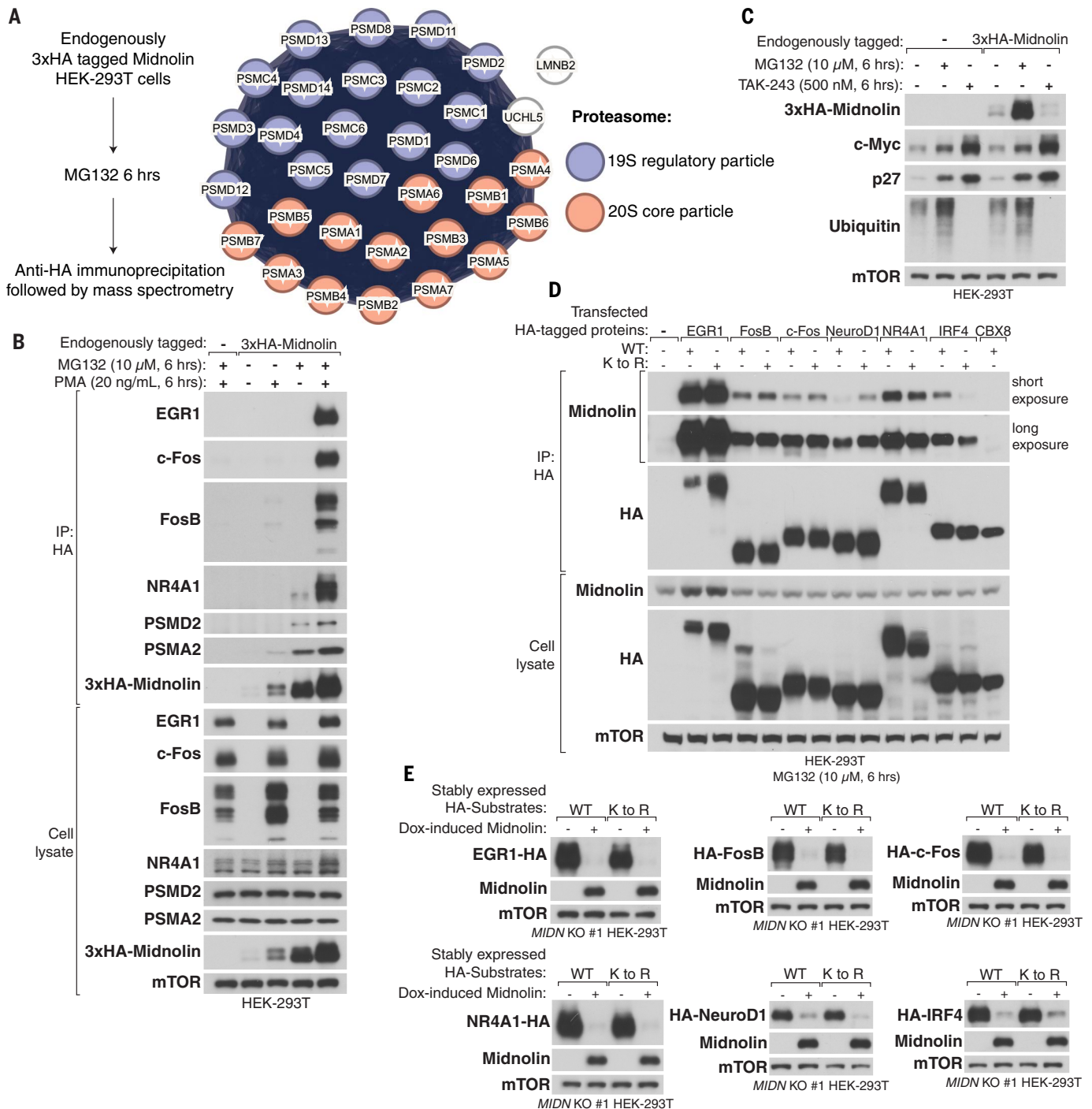
To gain insight into how midnolin interacts with the proteasome and its numerous substrates, we used AlphaFold to obtain a predicted structure of midnolin, which revealed three confidently predicted and highly conserved regions with defined structure (Fig. 5A and fig. S4, A and B) (26). Midnolin does not contain structural elements that are characteristic of RING- or HECT-type ubiquitin ligases (27) and does not contain a ubiquitin-binding domain characteristic of proteasomal processivity factors such as Rad23 or ubiquilin (28). Instead, midnolin contains a ubiquitin-like domain (Ubl) toward its N terminus. Additionally, midnolin contains two discontinuous regions, each composed of two predicted antiparallel β strands and two or three α helices, that appear to fold together to form a domain with internal symmetry. For reasons discussed below, we named this region of midnolin the “Catch” domain. Finally, midnolin contains a long α helix toward its C terminus, called α Helix-C, which includes a predicted nuclear localization sequence (NLS). Indeed, endogenous midnolin was largely located within the nucleus, and deletion of the predicted NLS, but not other regions of midnolin, resulted in its localization to the cytoplasm (fig. S5, A and B).

To determine whether these three regions are important for midnolin function, we transiently expressed wild-type and mutant versions of midnolin in *MIDN* KO HEK-293T cells stably expressing the GPS IRF4 or FosB reporters (Fig. 5, B and C). Although wild-type midnolin

potently promoted IRF4 and FosB destruction, point mutations of the Ubl or deletions of the Ubl, Catch, α Helix-C, or NLS domains abrogated midnolin function (Fig. 5C and fig. S6A).

We next performed coimmunoprecipitation experiments to identify midnolin domains that are required for its interaction with substrates and/or the proteasome. Point mutations or deletion of the Ubl domain did not disrupt the stable association of midnolin with EGRI or the proteasome (Fig. 5D). However, mutagenesis of the Ubl domain potentially increased midnolin levels, and these Ubl mutants were only marginally sensitive to MG132 (Fig. 5D). This suggests that the ubiquitination-independent degradation of midnolin that we observed previously (Fig. 4C) is dependent on its Ubl domain. By contrast, deletion of the NLS or entire C-terminal α helix revealed that this domain is necessary for midnolin to interact stably with the proteasome but not its substrates (Fig. 5D). This association with the proteasome was not affected by inhibition of the proteasome or E1 ubiquitin-activating enzymes (fig. S6B). When fused to maltose-binding protein (MBP), the midnolin helix conferred the ability to interact with the proteasome (Fig. 5E). Thus, the C-terminal midnolin helix is both necessary and sufficient to bind the proteasome and midnolin and, unlike the processivity factors Rad23 and ubiquilin, engages the proteasome stably independently of the Ubl domain (Fig. 5D) (29, 30).

Deletion of the regions that fold together to form the Catch domain (the N-terminal Catch1 and C-terminal Catch2 subdomains) abolished the interaction of midnolin with its substrates without affecting its ability to bind the proteasome (Fig. 5D). In growth-arrested NIH/3T3 cells in which the level of endogenous midnolin substrates was induced upon serum restimulation, the interaction of midnolin with its substrates also required the Catch domain (fig. S6C). To determine whether the Catch domain is both necessary and sufficient to engage midnolin substrates, we immunoprecipitated transfected wild-type, Catch domain-deleted midnolin or the Catch domain alone in HEK-293T cells and assessed the interaction with various substrates and proteasomal components. Deletion of the Catch domain abolished the interaction of midnolin with its substrates while retaining proteasome binding, and the Catch domain alone was sufficient to bind midnolin substrates (Fig. 5F). Catch1 and Catch2 are separated by a long, 111-amino acid unstructured sequence that is poorly conserved. We shortened this Catch1 and Catch2 linker to 10 amino acids (Δ Loop1), 16 amino acids (Δ Loop2), or 28 amino acids (Δ Loop3). These midnolin variants still interacted with substrates and promoted their degradation, indicating that the long stretch connecting Catch1 and Catch2 is largely dispensable (Fig. 5F and fig. S7, A and B). However, the length between Catch1 and Catch2 could not be too short,



inhibition but not by ubiquitin E1 inhibition. Immunoblotting was performed from wild-type and 3xHA-midnolin knock-in HEK-293T cells treated with 10 μ M MG132 or 500 nM TAK-243 for 6 hours. (D) Lysine-dependent ubiquitination on substrates is not necessary for midnolin interaction. Immunoblotting was performed from anti-HA immunoprecipitants of HEK-293T cells that were transfected with the indicated constructs, either wild-type or all lysine residues mutated to arginine residues (K-to-R mutants). Cells were treated with 10 μ M MG132 for 6 hours. CBX8 serves as a negative control as it is not targeted by midnolin. (E) Midnolin does not require lysine residues on substrates to promote degradation. Wild-type and K-to-R mutant substrates were stably introduced into *MIDN* KO HEK-293T cells using a cytomegalovirus (CMV) promoter. Then, midnolin expression was induced using doxycycline (100 ng/ml) for 2 days using a TRE promoter before lysis and immunoblotting.

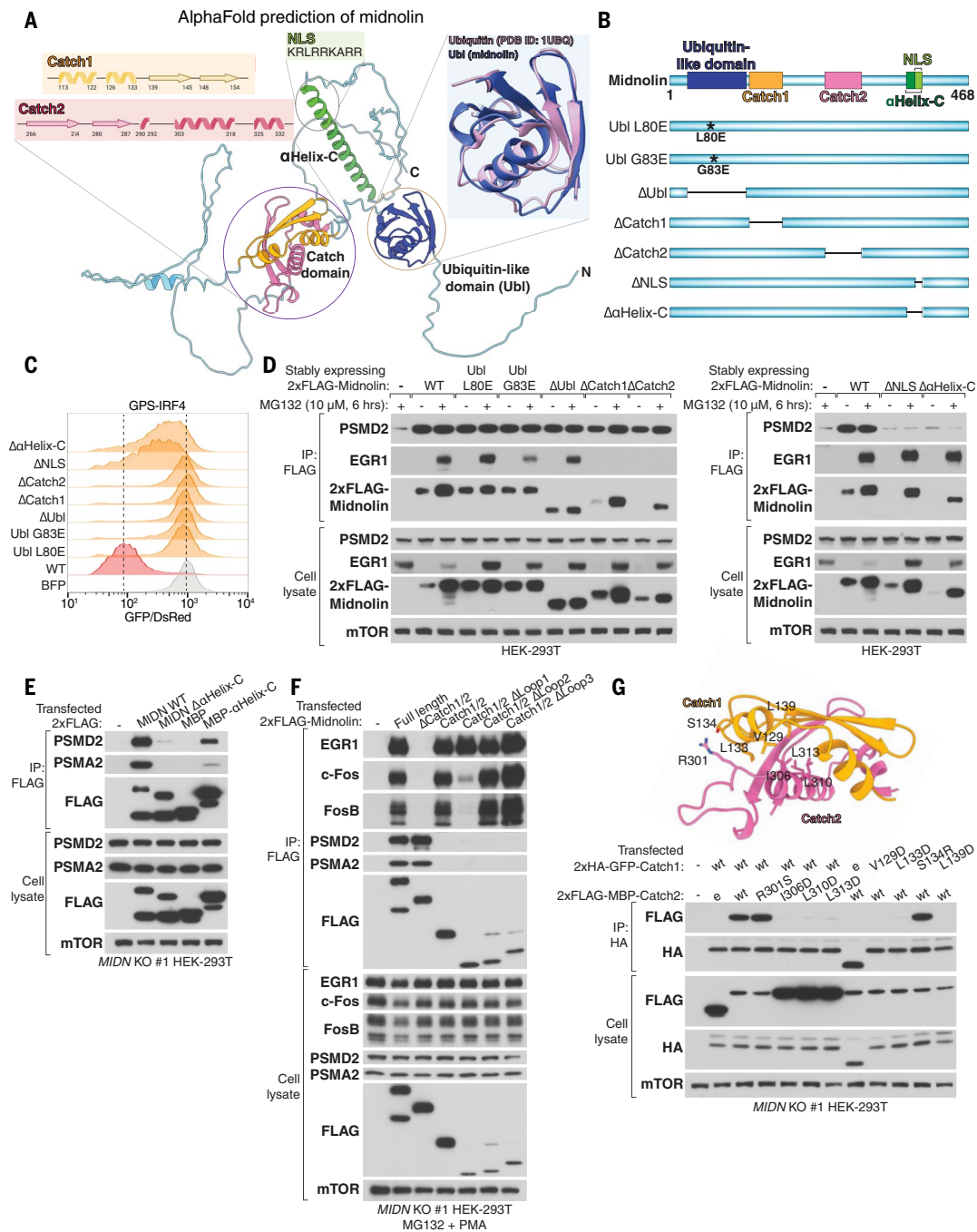


Fig. 5. Midnolin contains three regions that function in concert to promote proteasomal degradation of bound substrates. (A) Midnolin structure prediction by AlphaFold (Q504T8-F1) reveals three regions with defined structure (26). (B) Schematic representation of mutations (72) or truncations introduced into the midnolin cDNA. See the materials and methods for the truncation boundaries and regions used for sufficiency experiments. (C) Regions with defined structure are necessary for a functional midnolin. The GPS IRF4 reporter was stably expressed in MIDN KO HEK-293T cells, and a control BFP or wild-type and mutant versions of midnolin coexpressing BFP were transiently transfected before analyzing the GFP/DsRed ratio by flow cytometry. (D) The midnolin Catch domain is necessary for binding substrates, and the C-terminal α helix is necessary for proteasomal association. Immunoblotting was performed from anti-FLAG immunoprecipitants of HEK-293T cells stably expressing 2xFLAG-tagged midnolin using a CMV promoter. Cells were treated with 10 μM

MG132 for 6 hours. (E) The midnolin αHelix-C is sufficient to interact with the proteasome. Immunoblotting was performed from anti-FLAG immunoprecipitants of MIDN KO HEK-293T cells transfected with the indicated 2xFLAG-tagged proteins. (F) The midnolin Catch domain is sufficient to bind substrates. Immunoblotting was performed from anti-FLAG immunoprecipitants of MIDN KO HEK-293T cells transfected with the indicated 2xFLAG-tagged proteins. The 111-amino acid sequence between Catch1 and Catch2 was shortened to 10 amino acids (ΔLoop1), 16 amino acids (ΔLoop2), or 28 amino acids (ΔLoop3). Cells were treated with 10 μM MG132 and 20 ng/ml of PMA for 6 hours. (G) The Catch1 and Catch2 regions of midnolin interact when expressed as independent proteins. Immunoblotting was performed from anti-HA immunoprecipitants of MIDN KO HEK-293T cells cotransfected with 2xHA-GFP-Catch1 and 2xFLAG-MBP-Catch2 constructs, where “e” signifies empty 2xHA-GFP or 2xFLAG-MBP.

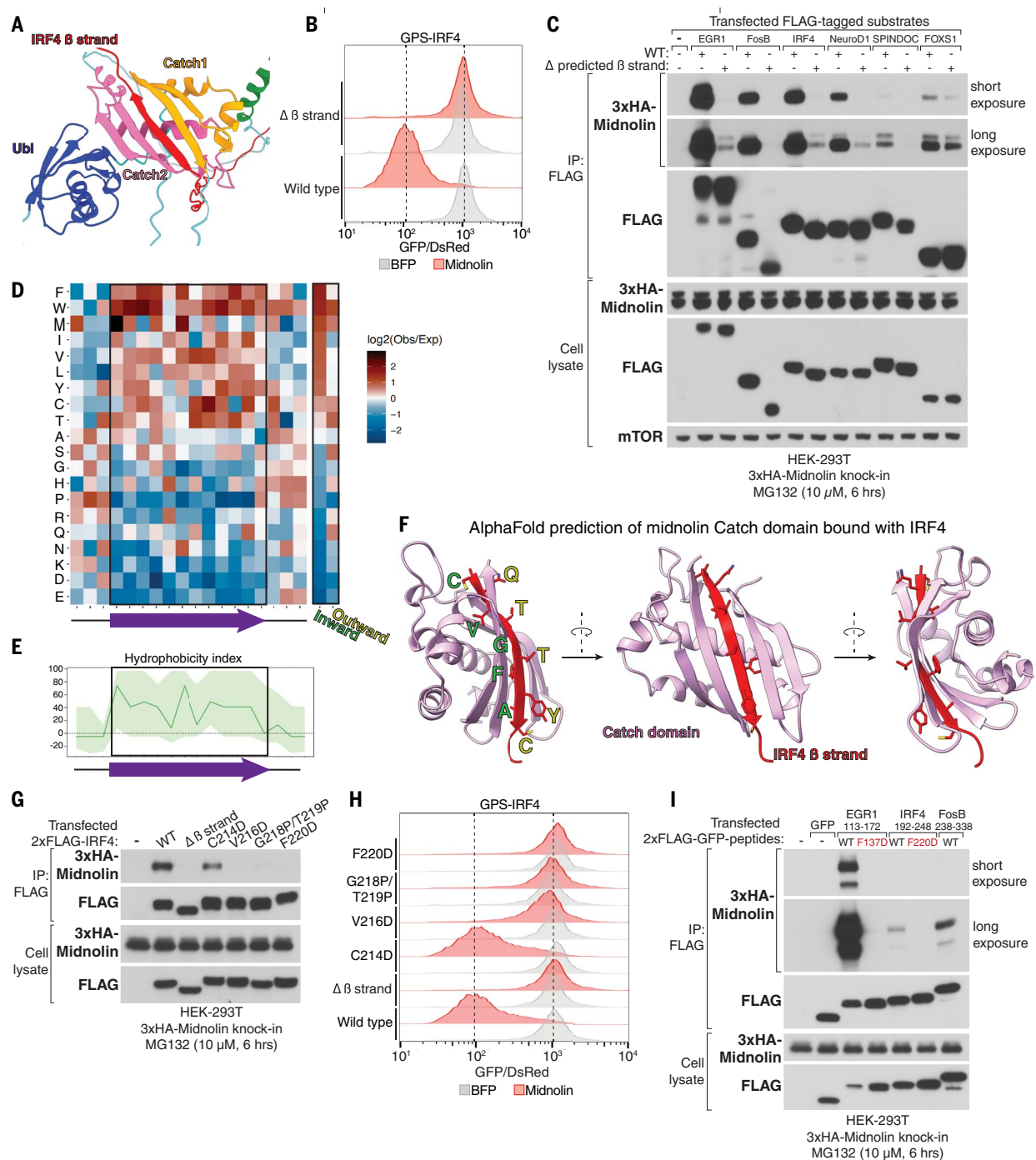


Fig. 6. Midnolin catches regions within its substrates that constitute a β -strand degron. (A) AlphaFold structure prediction of midnolin bound to its substrate IRF4 reveals an adopted β -strand capture model. (B) Midnolin requires the predicted β strand within IRF4 to promote degradation. The GPS IRF4 reporters were stably expressed in *MIDN* KO HEK-293T cells, and a control BFP or midnolin coexpressing BFP was transiently transfected before analyzing the GFP/DsRed ratio by flow cytometry. (C) Predicted β strands are necessary for interaction with midnolin. Immunoblotting was performed on anti-FLAG immunoprecipitants of 3xHA-midnolin knock-in HEK-293Ts transfected with 2xFLAG-tagged substrates. For FosB, the comparison is between the full-length protein and Δ FosB. Cells were treated with 10 μ M MG132 for 6 hours. See the materials and methods for the truncation boundaries. (D) Amino acid frequency of midnolin substrate β strands predicted by AlphaFold reveals a strong

preference for hydrophobic residues. “Inward” is defined by the residues buried within the Catch domain, and “Outward” is defined by the solvent-exposed residues. (E) The hydrophobicity of residues within the β strand was determined by a mean hydrophobicity index at pH 7 (70, 71) of residues immediately before, within, or immediately after the β strand. (F) AlphaFold structure prediction of the midnolin Catch domain bound to IRF4. (G) Hydrophobic β -strand residues buried within the Catch domain are required for midnolin interaction [similar assay as in (C)] but from cells transfected with the 2xFLAG-tagged IRF4 constructs. (H) Midnolin requires the hydrophobic β -strand residues buried within the Catch domain to promote degradation [similar assay as in (B)]. (I) Regions encompassing predicted β strand(s) are sufficient for conferring an interaction with midnolin [similar assay as in (C)] but from cells transfected with the indicated 2xFLAG-GFP-peptide fusions.

because the shortest linker (Δ Loop1, 10 amino acids) did attenuate the interaction of midnolin with certain substrates (Fig. 5F and fig. S7A). Thus, the linker between Catch1 and Catch2 may still be important for proper flexibility or folding of the Catch domain.

Given the importance of the Catch domain for binding substrates, we further validated the AlphaFold prediction that Catch1 and Catch2 fold together. This folding may be strongly driven by hydrophobicity, because the core of the Catch domain is composed exclusively of highly conserved hydrophobic amino acids (fig. S7C). To validate that Catch1 and Catch2 fold back to bind each other in a process driven by hydrophobicity, we expressed each separately by tagging Catch1 to 2xHA-GFP and Catch2 to 2xFLAG-MBP. We also generated a series of mutants for both Catch1 and Catch2 in which some hydrophobic residues predicted by AlphaFold to drive the interaction were changed to aspartic acid. As a control, we mutagenized a solvent-exposed residue on Catch1 (S134) and Catch2 (R301) because these were not predicted to contribute to the binding between Catch1 and Catch2. These epitope-tagged Catch1 and Catch2 constructs were expressed in *MIDN* KO HEK-293T, and 2xHA-GFP-Catch1 was immunoprecipitated. Indeed, Catch1 and Catch2 bound each other when expressed as independent proteins, and mutagenesis of the hydrophobic residues to aspartic acid abolished the interaction (Fig. 5G). This contrasts with mutagenesis of the solvent-exposed residues, which did not alter the Catch1-Catch2 interaction as anticipated. We also introduced these same mutations into full-length midnolin, and only mutagenesis of the hydrophobic residues abolished the ability of midnolin to bind with and promote the degradation of its substrates (fig. S7, B and D). The hydrophobic core was important for the function of the Catch domain, because mutagenesis of additional hydrophobic residues to aspartic acid attenuated the ability of midnolin to promote the degradation of its substrates, including IRF4 and FosB (fig. S7E).

Therefore, midnolin is primarily localized within the nucleus, associates with the proteasome using its long C-terminal α helix, binds substrates using its hydrophobic Catch domain, and contains a Ubl domain that is necessary to promote substrate degradation. Overall, these three regions of midnolin function in concert to promote ubiquitination-independent proteasomal degradation of bound substrates.

Midnolin “catches” regions within its substrates that constitute a β -strand degron

We wondered how midnolin achieves substrate selection through its Catch domain given its ability to promote the destruction of many diverse proteins. Canonically, E3 ubiquitin ligases bind short linear motifs within substrates, called degrons, in which the amino acid

side chains play crucial roles in determining substrate specificity (31–34). To gain insights into how midnolin achieves substrate selection, we used AlphaFold to predict the structure of the midnolin-substrate bound complex (26). The AlphaFold predictions for midnolin bound to IRF4 (Fig. 6A) revealed that a predicted unstructured region of native IRF4 (fig. S8A) formed a β strand upon binding to the midnolin Catch domain (fig. S8B), thereby completing a five-stranded antiparallel β -sheet tertiary structure. Consistent with this AlphaFold-predicted interaction, a small deletion within IRF4 that encompassed the predicted β strand abolished the ability of midnolin to promote IRF4 degradation (Fig. 6B).

To determine the generality of this β -strand capture mechanism, we performed the AlphaFold structure predictions for the 508 most destabilized proteins uncovered in the GPS ORFeome screen. The Protein Data Bank (PDB) files for these 508 predictions can be accessed on Dryad using the DOI 10.5061/dryad.m905qfv6g. Approximately 40% (205/508) of the proteins have predictions that are consistent with them being captured by midnolin (data S4). We systematically compared the AlphaFold-predicted structure of midnolin substrates in the native and midnolin-bound states. The regions predicted to be captured by midnolin are generally more unstructured than the rest of the same protein in the native state but have the potential to form a β strand upon binding to the Catch domain (fig. S8C). We validated these findings by introducing into several representative midnolin substrates small deletions that encompassed the predicted β strand and tested the ability of midnolin to interact with and promote the degradation of these mutants. In each case, deletion of the predicted β strand abrogated the ability of midnolin to both interact with substrates (Fig. 6C) and promote their degradation (fig. S9, A to D).

The AlphaFold predictions yielded several different modes of midnolin-FosB interaction, raising the possibility that the N and C terminus of FosB have the potential to form multiple different β strands that could be captured by midnolin. We generated various truncated forms of FosB to determine which regions were necessary for midnolin to promote degradation and found that the C-terminal 101 amino acids were required (fig. S10A). Truncation of the last 101 amino acids of FosB results in a naturally existing splice isoform called Δ FosB, which was shown to be significantly more stable than other Fos family members, although the molecular basis for this increased stability was unknown (35). Previous studies have shown that chronic and repeated exposure to drugs of abuse such as cocaine leads to week-long accumulation of Δ FosB protein expression in the nucleus accumbens, a brain region crucial for addiction (35, 36). Indeed, overexpression of

Δ FosB in neurons of the nucleus accumbens sensitizes animals to the effects of cocaine and may thus contribute to addiction (37). In contrast to full-length FosB, midnolin weakly interacted with and less effectively promoted the degradation of Δ FosB (Fig. 6C and fig. S10A). Our findings therefore provide a mechanistic explanation for the increased stability of Δ FosB. Nevertheless, Δ FosB is eventually degraded, and this may require the N terminus of FosB, which is also predicted by AlphaFold to form a β strand that can be captured by midnolin. Deletion of the predicted N-terminal β strand region within Δ FosB largely abolished its ability to be targeted for decay by midnolin (fig. S10B). Thus, a protein can contain more than one region that can be captured by midnolin.

Having identified sequences that mediate the midnolin-substrate interaction, we investigated whether specific amino acids were enriched or depleted over others within the predicted β strands captured by the midnolin Catch domain. Within these β strands, we observed a marked depletion of charged amino acids, including aspartic acid and glutamic acid, as well as proline (Fig. 6D), which is known to disrupt β strands (38). Instead, there was a strong enrichment for hydrophobic amino acids within the midnolin-induced β strands, which overall were significantly more hydrophobic than the average of all other regions within the same protein (Fig. 6E and fig. S10C). Once bound by midnolin, these hydrophobic β strand residues were predicted to be buried within the core of the Catch domain (inward), whereas charged amino acids tended to point outward and were solvent exposed (Fig. 6, D and F, and fig. S10D). The enrichment for hydrophobicity within the β strands is consistent with the fact that the core of the Catch domain is also highly hydrophobic and required for catching hydrophobic regions within substrates. To validate these predictions, two residues (G218 and T219) at the center of the predicted IRF4 β strand were mutagenized to proline to potentially disrupt β -strand formation, or the hydrophobic residues buried within the interior of the Catch domain (V216, and F220) were mutagenized to aspartic acid to disrupt potential hydrophobic interactions. Consistent with the AlphaFold predictions, both the introduction of prolines and mutagenesis of the hydrophobic residues to aspartic acid within the β strand abolished the ability of midnolin to interact with (Fig. 6G) and promote the degradation of IRF4 (Fig. 6H). Similar results were obtained after mutagenesis of the corresponding residues within the EGR1-adopted β strand (fig. S10, E and F).

We next tested whether midnolin could interact with and promote the degradation of GFP fused to a short sequence containing the β -strand degron(s) within substrates. Midnolin interacted with (Fig. 6I) and promoted the degradation of GFP fused to short stretches within EGRL, IRF4,

and the C-terminal tail of FosB that was dependent on the hydrophobicity of the predicted β strand (fig. S10, G and H). Thus, the β strands predicted by AlphaFold are necessary and sufficient to interact with midnolin for proteasomal degradation.

We conclude that midnolin achieves substrate selection through a general mechanism: Captured regions within substrates have the ability to form a β strand that is biochemically compatible with the hydrophobic core of the Catch domain.

Discussion

In this study, we identified a protein called midnolin that targets stimulus-induced transcription factors such as c-Fos, FosB, EGFR, NR4A1, and IRF4 to the proteasome for degradation. Disrupting midnolin function in various cell types increases the peak abundance of these transcription factors and prolongs their expression. It is not uncommon for a protein to be targeted for proteasomal degradation by multiple mechanisms, and these stimulus-responsive transcription factors may not be targeted for degradation solely by midnolin. Rather, it is possible that these proteins are also targeted by a ubiquitination-dependent pathway that functions in parallel with midnolin and could be the primary mechanism of degradation in some contexts. Indeed, it has been reported that Fos family members are targeted by both ubiquitination-dependent and -independent mechanisms (7). We found that midnolin is induced by diverse stimuli, and its induction may act as a post-translational feedback circuit to limit the time course of expression of these stimulus-responsive transcription factors. Through a gain-of-function genetic screen, we identified a large group of potential targets of midnolin strongly enriched for nuclear proteins, especially transcriptional regulators, revealing that midnolin functions broadly to promote the degradation of proteins in the nucleus, where midnolin itself is predominantly localized.

The biological functions of midnolin are likely complex. Many of its substrates play central roles in the nervous and immune systems, and thus it will be important to establish the physiological function of midnolin *in vivo*. Midnolin was initially discovered because of its strong induction in the midbrain early during embryonic development (39). However, how midnolin expression is induced both during development and in cultured cells is currently unclear. Midnolin may have evolved to integrate various upstream stimuli and shape the proteome swiftly as a crucial response to the initial stimuli. Many midnolin substrates, including IEG proteins and lineage-specific transcription factors, undergo a transient burst of expression either in response to a particular stimulus or during a specific stage of development, and thus the prolonged expression of these transcription

factors could be detrimental to organismal physiology. Indeed, previous studies have shown that chronic and repeated exposure to drugs of abuse such as cocaine leads to week-long accumulation of Δ FosB, which plays a crucial role for addiction in the nucleus accumbens of the brain (35–37). Our finding that Δ FosB is resistant to midnolin-dependent degradation provides a glimpse into the role that midnolin could play in brain function. Given that many IEG proteins are efficiently targeted for degradation by midnolin and that the precise expression of IEGs is critical for learning and memory (1, 3, 40), it is possible that disrupting or boosting midnolin function could affect the ability of animals to efficiently learn and store information in the brain.

IRF4, another midnolin substrate, is a lineage-specific transcription factor that is essential for the function and homeostasis of mature B and T cells and is an oncogenic driver of multiple myeloma (15, 16, 41). IRF4 protein expression is potently induced by diverse stimuli, including T cell receptor signaling and cytokines (42–45). How the IRF4 protein returns to baseline after stimulation was unknown, and our finding that IRF4 is potently targeted for degradation by midnolin may provide insights into the function of midnolin in the immune system. Taken together, these findings suggest that midnolin may serve as a key regulator that determines the precise expression kinetics of stimulus-induced transcription factors by controlling their protein stability in various cell types or tissues. In principle, midnolin could be used to target different proteins under different circumstances. For example, in flies, it was reported that a midnolin ortholog, Stuxnet, is cell cycle regulated and promotes Pc protein degradation in mitosis during development (14).

We found that midnolin promotes the degradation of its targets in a proteasome-dependent but ubiquitination-independent manner. This is supported by multiple lines of evidence. Removal of lysine residues from many midnolin targets did not abrogate the ability of midnolin to bind with and promote their destruction. A caveat to this interpretation is that ubiquitination can occur on the N-terminal amine of the first amino acid if it is not acetylated or, more rarely, on other residues such as cysteine, serine, or threonine (24). However, in contrast to the effects of proteasomal inhibition, blocking the E1 ubiquitin-activating enzyme did not abrogate midnolin function while stabilizing canonical substrates of the ubiquitin-proteasome system. These experiments allowed us to conclude that midnolin does not require ubiquitination for its degradative function. Instead, midnolin engages substrates using its Catch domain, which binds a hydrophobic region capable of β -strand formation that functions as a degron. Midnolin associates with the proteasome using its long, C-terminal α helix and contains an N-terminal

ubiquitin-like domain that is essential to promote the degradation of bound substrates. We hypothesize a model whereby the concerted action of these three regions of midnolin allows for the ubiquitination-independent proteasomal degradation of midnolin-bound proteins (Fig. 7).

Previous work demonstrated that ornithine decarboxylase is targeted directly to the proteasome for degradation through a C-terminal unstructured sequence (46–49). However, the regions within substrates captured by midnolin are unlike any others previously described for E3 ubiquitin ligases. The midnolin degron appears to be generally unstructured but has the potential to form a β strand upon binding midnolin, with aliphatic residues of the degron buried within the hydrophobic core of the Catch domain. The integration of the β -strand degron into the Catch domain appears to complete a five-stranded antiparallel β -sheet structure. The somewhat degenerate nature of these hydrophobic degrons in various substrate proteins is likely explained by the fact that β sheets are stabilized not only by side chain interactions but also by backbone hydrogen bonding (50), which may reduce the need for specific amino acid interactions. A region with the propensity to form a β strand that is also biochemically compatible with the hydrophobic core of the Catch domain may be present in many proteins, thereby explaining how midnolin recognizes a diverse set of proteins. Given the ubiquity of such β strands as structural elements of proteins, midnolin recognition of unfolded proteins could behave as a general quality control mechanism.

How midnolin initiates the degradation of bound substrates is not completely understood mechanistically. We do not know if midnolin interacts with its targets before binding to the proteasome or if it associates with the proteasome constitutively and then recruits its substrates, thus defining a new subclass of proteasomes in the nucleus. We favor the latter possibility, because a unique feature of midnolin is that it interacts stably with the proteasome using a C-terminal α helix but not its Ubl domain. This is unlike the processivity factors Rad23 and ubiquilin, which bind ubiquitinated cargo and use their Ubl domain to interact with the proteasome (29, 30, 51–53). How the midnolin α helix binds the proteasome is currently unclear, and we do not yet understand how the Ubl functions. However, the Ubl domain of midnolin is necessary for the degradation of bound substrates, and it is noteworthy that midnolin itself is efficiently degraded by the proteasome in a ubiquitination-independent manner that requires the Ubl domain. Whether midnolin is reused or being degraded along with the substrate remains to be determined. We hypothesize that when midnolin interacts with a substrate, a conformational change occurs that allows the proteasome to recognize the Ubl

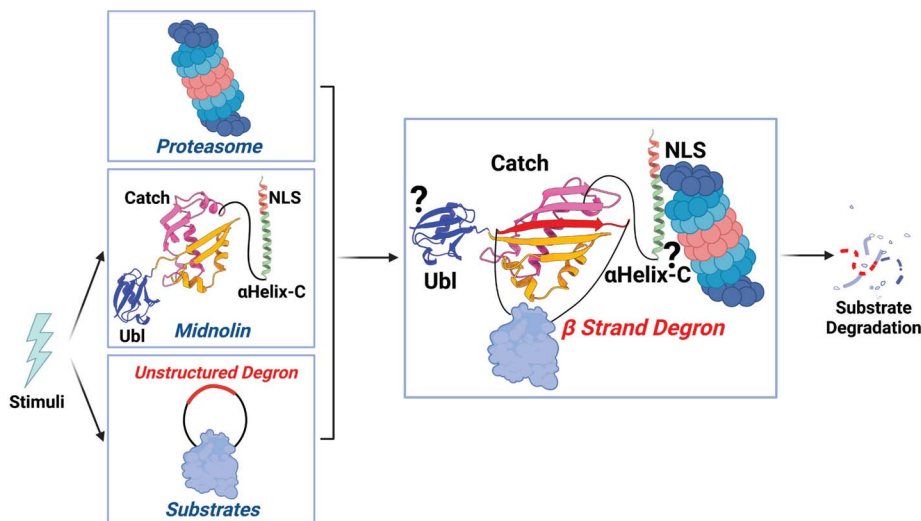


Fig. 7. Model for how midnolin functions to promote ubiquitination-independent proteasomal degradation. Midnolin is induced by growth factors and neurological stimuli, and its overexpression is sufficient to cause the degradation of its targets, including transcription factors such as c-Fos, FosB, ERG1, NR4A1, IRF4, and potentially many other proteins within the nucleus, where midnolin primarily resides. The degradation of its substrates does not require ubiquitination. Instead, midnolin uses its Catch domain to bind unstructured hydrophobic regions within substrates that have the potential to form a β strand that functions as a midnolin degron. Midnolin associates with the proteasome using its long C-terminal α helix and promotes the destruction of Catch-bound substrates through its N-terminal ubiquitin-like domain. Structures of the midnolin domains are derived from AlphaFold predictions. How the C-terminal α helix of midnolin binds the proteasome, whether a conformational change occurs after substrate binding, and how the ubiquitin-like domain confers degradative activity require further investigation (figure created with [BioRender.com](https://www.bio-render.com/)).

domain transiently to promote the degradation of the bound substrate with or without midnolin also being degraded. Structural and biochemical analyses are required to deepen our understanding of this noncanonical docking and degradative mechanism.

Our results suggest that the midnolin-proteasome pathway may represent a general mechanism by which the proteasome bypasses the traditional ubiquitination system to achieve selective degradation of many nuclear proteins. It has been reported that in bacteria, which do not contain the ubiquitin-proteasome system, a hierarchy of adaptors mediate selective degradation of diverse proteins by the proteasome-equivalent ClpXP protease complex (54, 55). It will be of interest to determine whether, in the course of evolution, additional proteins have evolved to recruit proteins directly to the proteasome for degradation.

Materials and Methods

Cell culture

HEK-293T (ATCC, CRL-3216, RRID: CVCL_0063) and NIH/3T3 (ATCC, CRL-1658, RRID: CVCL_0594) cells were cultured at 37°C and 5% CO₂ in Dulbecco's modified Eagle's medium (DMEM) (Thermo Fisher Scientific, I1965118) supplemented with 100 units/ml penicillin, 0.1 mg/ml streptomycin (Thermo Fisher Scientific, 15070063), and 10% fetal bovine serum (Cytiva, SH30088.03). Ramos B cells (ATCC, CRL-1596, RRID: CVCL_0597)

were cultured in RPMI 1640 medium (Thermo Fisher Scientific, A1049101) supplemented with 100 units/ml penicillin, 0.1 mg/ml streptomycin, and 10% fetal bovine serum. NIH/3T3 cells were starved overnight of serum and restimulated the following day with 20% serum for the indicated time points.

Animals were handled according to the protocol (IS00000074-6) approved by the Harvard University Office of the Institutional Animal Care and Use Committee, HMA Standing Committee on Animals and were in accordance with federal guidelines. Mouse cortical neurons were isolated and cultured as described previously (56). In short, embryonic cortices from wild-type C57BL/6NcrJ mice (Charles River Laboratories strain number 027, five to 10 embryos, both males and females) were dissected at embryonic day 16.5 (E16.5) and dissociated with papain (Sigma Aldrich, 10108014001). After terminating the papain digestion with ovomucoid (trypsin inhibitor from Worthington), cells were triturated gently through a P1000 pipette before passing through a 40- μ m filter, and then plated on cell culture dishes coated with poly-D-lysine (20 μ g/ml) and laminin (4 μ g/ml). The culture medium used for neurons was Neurobasal medium (Gibco) that contains 2% B27 supplement, penicillin-streptomycin (50 U/ml penicillin and 50 U/ml streptomycin), and glutaMAX (1 mM). The neurons were cultured at 37°C and 5% CO₂, treated with corres-

ponding viruses at 3 days in vitro (DIV) while adding fresh culture medium at the same time (35% of total volume), silenced on 10 DIV overnight by the addition of 1 μ M tetrodotoxin (TTX; Abcam, ab120055) and 100 μ M AP5 (Thermo Fisher, 01-061-0), and harvested at 11 DIV after treatment with KCl stimulation buffer composed of 52.8 mM KCl, 0.62 mM CaCl₂, 0.31 mM MgCl₂, and 3.1 mM HEPES, pH 7.4, for the indicated times.

Cells were treated with 20 ng/ml PMA (Thermo Fisher Scientific, J-63916-MA), 10 μ M MG132 (Selleckchem, S2619), or 500 nM TAK-243 (Selleckchem, S8341) from 1000 \times stock solution in dimethylsulfoxide (DMSO) for 6 hours unless stated otherwise.

Plasmids and cloning

The genome-wide CRISPR-Cas9 single-guide RNA (sgRNA) root library (five sgRNAs/gene, 94,335 sgRNAs total) was used previously, and the sgRNA information can be found in data S1 (57). The barcoded GPS ORFeome expression library was generated previously (13). The plasmids for human cDNAs containing a stop codon and conferring kanamycin resistance were obtained from the Ultimate ORF Clone collection (Thermo Fisher Scientific) in the form of Gateway entry clones: MIDN (IOH62653, BC094778.1), FOSB (IOH62162, NM_006732.2), FOS (IOH5624, NM_005252.3), ATF2 (IOH37849, NM_001880.2), CREB3 (IOH14437, BC009402.2), CREB5 (IOH53714, NM_001016661.1), ATF3 (IOH6465, NM_001674.2), BATF2 (IOH13295, BC012330.1), COMMD9 (IOH12792, NM_014186.3), C11ORF31 (IOH58679, NM_170746.2), ZNF621 (IOH44483, NM_198484.3), SERTAD2 (IOH42292, NM_014755.2), LMX1A (IOH34878, NM_177398.2), LMX1B (IOH34707, NM_002316.2), HOXD3 (IOH5660, NM_006898.4), CHCHD2 (IOH3869, NM_016139.2), FNDC3B (IOH10620, BC012204.1), SOX12 (IOH40697, NM_006943.2), TAX1BP3 (IOH13074, NM_014604.2), PAX4 (IOH34754, BC074761.2), FOXA3 (IOH10014, NM_004497.2), STYX (IOH10157, NM_145251.3), ZNF764 (IOH6451, NM_033410.2), RelB (IOH11686, NM_006509.2), PRRX1 (IOH36664, NM_006902.3), IRF1 (IOH2022, NM_002198.2), IRF2 (IOH10126, NM_002199.3), IRF8 (IOH42114, NM_002163.2), IRF9 (IOH28745, NM_006084.4), MYC (IOH2954, P01106), SPINDOC (IOH28799, NM_138471.1), PPDPF (IOH4080, NM_024299.2), PAX8 (IOH3823, NM_003466.3), FOXS1 (IOH13387, NM_004118.3), NEUROD1 (IOH3394, NM_002500.2), MIER2 (IOH40210, NM_017550.1), IRF4 (IOH12141, NM_002460.2), GATA1 (IOH57792, NM_002049.3), CITED1 (IOH5542, BC004240.1), and XRCCI (IOH40644, NM_006297.2).

The plasmids for human cDNAs lacking a stop codon and conferring spectinomycin resistance were obtained from the Human ORFeome library V8.1 (Dana Farber Cancer Institute) in the form of Gateway entry clones: EGFR (ORF_ID no. 14665, BC073983.1) and NR4A1 (ORF_ID no. 292, BC016147.1).

CBX4 and hemagglutinin (HA)-tagged wild-type or K-to-R mutated cDNA were generated by synthesis using Integrated DNA Technologies (IDT) with attB1 and attB2 overhangs for cloning into the pDONR221 (Thermo Fisher Scientific, 12536017) through a BP recombination reaction (Thermo Fisher Scientific, 11789020) to generate the entry clone. Similarly, the following attB1 and attB2 overhangs we included in primers to generate fragments for sufficiency experiments by polymerase chain reaction (PCR) for cloning into the pDONR221: attB1, GGGGACAAGTTTG-TACAAAAAAGCAGGCTTAGccacc; attB2, GGGGACCACTTTGTACA-AGAAAGCTGGGTA.

Entry clones were mutagenized by PCR using the Q5 Site Directed Mutagenesis kit (NEB, E0554S) and the primers for mutagenesis were designed using the NEBaseChanger program.

The midnolin amino acid sequence used was as follows: MEPQPGGARSCRAGPAGGACELG-PAEAEAPMSLAIHSTTGTRYDLAVPPDEIVEG-LRKRLSQRLKVPKERLALLHKDTRLSSGKL-QEFGVGDGSKLTLVPTVEAGLMSQASRPEQ-SVMQALESLTETQVSDFLSGRSPLTLALRV-GDHMMFVQLQLAAQHAPLQHRHVLAAA-AAAAAARGDPSIASPVSSPCRPVSSAARVPP-VPTSPSPASPITAGSFRSHAASITTCPEQM-DCSPTASSASPGASTTSTPGASPAPRSRKP-GAVIESFVNHAPGVFSGTFSGLTHPNCQD-SSGRPRRDIGITLQILNDLLSATRHYQGMPP-SLAQLRCHAQCSPASPAPDLAPRTTSCCKLT-AAPSASLLQGQSQIRMCKPPGDRLRQTENR-ATRCKVERLQLLLQKRLRRKARRDARGP-YHWSPSRKAGRSDDSSSSGGGSPSEASGLG-LDFEDSVVKPEANPDIKSEFVVA

Midnolin regions for truncations or sufficiency experiments were as follows: Δ Ubl, residues 31 to 105; Δ Catch1, residues 112 to 156; Δ Catch2, residues 266 to 332; Δ NLS, residues 402 to 413; $\Delta\alpha$ Helix-C, residues 377 to 413; α Helix-C region fused to MBP, residues 360 to 432; Catch domain alone for sufficiency experiment, residues 102 to 334; Δ Loop1, residues 160 to 260; Δ Loop2, residues 163 to 257; Δ Loop3, residues 169 to 251; Catch1 fused to 2xHA-GFP, residues 107 to 166; Catch2 fused to 2xFLAG-MBP, residues 254 to 337; FosB truncations: deletion1, residues 2 to 42; deletion2, residues 43 to 82; deletion3, residues 83 to 122; deletion4, residues 123 to 149; deletion5, residues 150 to 237; Δ FosB, residues 238 to 338; predicted β strand truncations: FOXS1, residues 245 to 260; CBX4, residues 538 to 558; NEUROD1, residues 277 to 288; SPINDOC, residues 314 to 328; IRF4, residues 208 to 229; FOSB (N-terminal β strand), residues 67 to 75; EGR1, residues 128 to 145; β -strand sufficiency peptides: EGR1, residues 113 to 172; IRF4, residues 192 to 248; FosB, residues 238 to 338.

Entry clones were subcloned into the following lentiviral Gateway destination vectors using an LR recombination reaction (Thermo Fisher Scientific, 11791100): pHAGE-GPS 3.0 (13), pHAGE-GPS 3.2 (58), pHAGE-CMV-2xFLAG-

N (this paper), pHAGE-CMV-2xHA-N (this paper), pHAGE-CMV Puromycin (59), pHAGE EF1 α BFP (this paper), CMV-C-2xFlag expression vector (Addgene, 118372), pHAGE TRE Blasticidin (this paper), pHAGE-CMV-2xHA-GFP-N (this paper), pHAGE-CMV-2xFLAG-GFP-N (this paper), and pHAGE-CMV-2xFLAG-MBP-N (this paper). The pInducer20 mouseCD19 (59) plasmid was used to generate dox-on responsive HEK-293T cells.

Lentiviral CRISPR-Cas9 vectors containing the sgRNA of interest were cloned by first digesting the backbone lentiCRISPRv2 (Addgene, 52961) using BsmBI (NEB, R0739S). Then, sgRNA oligos containing CACC or AAAC overhangs were obtained from IDT, phosphorylated and annealed together, and ligated into the linear backbone by T4 (NEB, M0202S) ligation. Sequences are as follows: nontargeting sgControl, GTATTACTGATATTGGTGGG; human sgMIDN #1, GAAGCTGCAGGAGTTCGGCC; human sgMIDN #2, GCTGACCTTGGTACCCACCG; and mouse sgMIDN, GCGAGCTGAACACGGCCA.

Lentivirus production

Lentivirus was generated by transfecting HEK-293T cells using PolyJet (SignaGen, SL100688) following the manufacturer's instructions with plasmids encoding Tat, Rev, Gag-Pol, and VSV-G and lentiviral transfer vectors. Specifically, plasmid DNA was diluted into DMEM lacking supplements, and 3 μ l of PolyJet reagent was used per 1 μ g of plasmid DNA. One day after transfection, the medium was removed and the cells were supplemented with fresh complete culture medium. The lentiviral supernatant was collected 48 and 72 hours after transfection, passed through a 0.45- μ m filter, and either applied directly to cells or stored at -80°C for later use. For most experiments, lentivirus was packaged in six-well plates. For library preparations, lentivirus was packaged in eight 15-cm plates using 13 μ g of total DNA per plate for transfection, pooled, concentrated using the lenti-X concentrator (Takara, 631232), and aliquoted.

Midnolin overexpression and flow cytometry

Cells were seeded in six-well plates at 200,000 cells/well and transfected 2 days later using Polyjet with EF1 α midnolin coexpressing BFP or BFP alone as a negative control. The medium was changed 1 day after transfection, and cells were analyzed 2 days after transfection.

Cells were prepared for flow cytometry by aspirating old media and rinsing cells once with phosphate-buffered saline (PBS). The cells were detached using 0.05% trypsin at room temperature, and the trypsin was neutralized using fresh complete media. The cells were then analyzed on a CytoFLEX S flow cytometer (Beckman Coulter, V2-B2-Y3-R2 version C09762) and the CytExpert software (Beckman Coulter) was used to collect flow cytometry data. All flow cytometry data were analyzed using

FlowJo software. For FACS, a Sony MA900 was used for routine sorting of single clones, and a MoFlo Astrios (Beckman Coulter) instrument was used to collect cells for the CRISPR-Cas9 and GPS ORFeome screens.

Generating doxycycline-inducible HEK-293T cells

Wild-type and MIDN KO HEK-293T cells were infected with lentivirus encoding the pInducer20 system expressing mouse CD19 as a doxycycline-inducible marker for cell surface staining. After infection, the cells were treated with doxycycline (100 ng/ml) for 2 days and then stained on the cell surface using phycoerythrin (PE) antimouse CD19 antibody (BioLegend, 152407, RRID: AB_2629816) for 30 min using 1 μ l of antibody diluted in 100 μ l of medium containing 1 million cells. The cells were rinsed twice with PBS before sorting for the PE-positive population. The sorted cells were allowed to expand for >1 week before being restained using PE antimouse CD19 antibody in the absence of doxycycline induction. The PE-negative population was sorted, and the cells were expanded before another round of staining and sorting for the PE-negative population. This allowed for a population of cells that responded to doxycycline with minimal leakiness. Finally, lentivirus encoding the pHAGE TRE-midnolin was infected into these MIDN KO HEK-293T cells and selected with blasticidin to allow for stable, doxycycline-inducible expression of midnolin.

EGR1 and FosB CRISPR-Cas9 screens

Genome-wide CRISPR-Cas9 screens were performed to uncover regulators of EGR1 and FosB protein stability. Specifically, the plasmid library was packaged into lentivirus by transfecting HEK-293T cells using PolyJet as described earlier, and the lentivirus was titered to obtain a multiplicity of infection \sim 0.3. HEK-293T cells were generated to express the GPS 3.0 FosB or GPS 3.2 EGR1 reporters by selecting using hygromycin (200 μ g/ml). These cells were then transduced with the titered CRISPR-Cas9 genome-wide Root library lentivirus at a multiplicity of infection (MOI) of \sim 0.3 to maintain a 500 \times representation throughout. Cells were selected 48 hours after transduction for 7 days using puromycin (2 μ g/ml) to remove uninfected cells. On the ninth day of puromycin selection, the 95th percentile most stable cell population was collected based on the GFP/DsRed ratio by FACS using a MoFlo Astrios instrument (Beckman Coulter). Additionally, the unsorted input cells were collected based on the number of cells collected in the enriched population. Collected cells were rinsed once with PBS, pelleted, and stored at -80°C .

Midnolin GPS ORFeome screen

The GPS ORFeome screen was performed as described previously (13) with some modifications. Sufficient cell numbers were used to

maintain at least a 300-fold coverage of the library throughout. The library was packaged into lentivirus and used to transduce *MIDN* KO HEK-293T at a MOI of 0.2. Two days after transduction, the HEK-293T cells were treated with 2 µg/ml puromycin for 6 days to remove uninfected cells, passaging the library once in between the selection period. The library-expressing cells were plated at 4 million cells/plate in a 15-cm dish and transfected 2 days later using Polyjet with 8 µg of DNA from *EF1α*-midnolin coexpressing BFP or BFP alone as a negative control. The cells were harvested 2 days after transfection and sorted into six stability bins based on the GFP/DsRed ratio by FACS using a MoFlo Astrios instrument (Beckman Coulter). The sorting gates were established using the BFP control to ensure that one-sixth of the population was collected per bin. Once the control populations were collected, the cells overexpressing midnolin were partitioned using the exact same sorting and gating settings as the control. The collected cells from each stability bin were rinsed once with PBS, pelleted, and frozen at -80°C for at least 12 hours.

Deconvolution of the pooled screens

Cell pellets were thawed and genomic DNA was harvested using a Gentra Puregene Core Kit (Qiagen). The sgRNAs or barcodes were then amplified by PCR using all the genomic DNA as a template (4 µg of DNA per reaction) to include stagger sequences and Q5 Hot Start High-Fidelity DNA Polymerase from NEB. A second round of PCR was performed using the clean PCR1 product to add the Illumina P5 and P7 adapter sequences. PCR2 samples were cleaned, pooled in the correct ratio, and sequenced on a NextSeq 500 instrument. The abundance of sgRNAs or barcodes were extracted from the raw sequencing data using Cutadapt (60) and mapped onto the reference library using Bowtie2 (61).

MAGECK was used to determine the enrichment of sgRNAs in the 95th percentile relative to the input population (62). The MAGECK score plotted on the *y*-axis (Fig. 1, B and C) represents the negative log₁₀ of the “pos|score” value generated by MAGECK.

For the GPS ORFeome analysis, the abundance of each ORF was corrected to account for sequencing depth and a protein stability index (PSI) score between 1 (most unstable) and 6 (most stable) was calculated using the following formula for each extracted ORF:

$$PSI = \sum_{i=1}^6 Ri * i$$

where *i* is the number of the stability bin denoted as an integer and *Ri* is the Illumina read proportion extracted from the bin *i*. The change in protein stability between midnolin and BFP is denoted as the difference in PSI (ΔPSI).

Gene set enrichment of GPS ORFeome hits

Gene set enrichment analysis (GSEA) was performed with GSEAPreranked (63) (v4.3.2) using rank weights derived from GPS ORFeome ΔPSI values as input. These were tested for enrichment across the Human Molecular Signatures Database (64) (MSigDB v2022.1.Hs) C5 Gene Ontology collection (i.e., GO:BP, GO:MF, and GO:CC). The classic Kolmogorov-Smirnov scoring scheme was used with 10,000 permutations and excluded gene sets with <10 or >1000 entries when intersected with the list of GPS ORFs.

Generating *MIDN* KO cells

To generate isogenic single clones lacking midnolin, HEK-293T cells were transfected with the lentiCRISPRv2 BFP plasmid encoding the given sgRNA of interest using Polyjet. Several days after transfection, the BFP-positive cells were collected as single cells into 96-well plates using FACS. The single clones were allowed to expand for 2 weeks before screening for a KO phenotype by immunoblotting and next-generation sequencing of the genomic DNA locus encompassing the cut site (fig. S11A).

To generate a population-level depletion of midnolin in mouse NIH/3T3 fibroblasts, cells were transduced with lentivirus encoding the given mouse lentiCRISPR v2 sgRNA coexpressing puromycin. Three days after transduction, cells were selected by 2 µg/ml puromycin for 5 days and expanded for further analysis.

To generate a population-level depletion of midnolin in primary cortical neurons, cells were transduced with lentivirus encoding the given mouse lentiCRISPRv2 sgRNA coexpressing puromycin.

To generate a population-level depletion of midnolin in Ramos B cells, the cells were transduced by spinfection with lentivirus encoding the given lentiCRISPRv2 sgRNA#1 coexpressing BFP. Specifically, the cells were incubated with lentivirus for 30 min with centrifugation at 2000 rpm at room temperature. The cells were then allowed to expand for 6 days after transduction, and the BFP-positive cells were collected by FACS.

Generating 3xHA-MIDN knock-in HEK-293T cells

To generate an endogenous 3xHA-tagged midnolin cell line, we used homology-directed repair and CRISPR-Cas9. We reasoned that an N-terminal epitope tag would be tolerable, because an N-terminal tagged midnolin transgene could interact with substrates and promote their degradation. To establish the knock-in line, the following custom Alt-R sgRNA and single-stranded DNA (ssDNA) homology-directed templates were generated by synthesis from IDT. The sgRNA template was: rCrCrGrGrCrUrGrCrGrCrUrCrCrArUrCrCrGrUrUrArArGrArGrCrUrArUrGrCrUrGrArArArCrArGrCrArUrArGrCrArArGrUrUrArArArArAr-

GrGrCrUrArGrUrCrCrGrUrUrArUrCrArArCrUrUrGrArArArArArGrUrGrGrCrArCrGrArGrUrCrGrUrGrCrUrUrUrUrUrU. The ssDNA template was: CGGCGCCCGCCGCCCCAGCCC-CCCAGCGCGCGCCGGGATGTATCCCTATGACGTGCCTGATTACGCCGCGGAGGATCCT-ACCCCTATGATGTGCCTGACTACGCTGGCAGCGGAGGATACCCTTATGATGTGCCTGATTATGCTGGAGGTGGAGGTAGTGAGCCGACGCCGCGCGCCCGGAGCTGCCGCGCGG.

spCas9, sgRNA, and ssDNA template were introduced to cells by nucleofection. Specifically, per nucleofection of 100,000 cells in Lonza strip nucleofector system (V4XC-2032), 0.8 µl of 62.1 µM spCas9 (Aldevron, 9212-0.25MG), 0.8 µl of 100 µM sgRNA (Alt-R from IDT), 0.25 µl of 10× buffer 3.1 (NEB, B6003S), and 0.65 µl of H₂O were mixed to bring the final volume to 2.5 µl per nucleofection and incubated Ribonucleoprotein (RNP) at room temperature for 30 min. Making a master mix to troubleshoot the ssDNA template concentration is recommended to avoid small volumes. Then, 2 µl of the RNP was added to 100,000 HEK-293T cells resuspended in 16.4 µl of Nucleofector solution plus 3.6 µl of supplement. Donor DNA was added directly to this solution at a final concentration of 500 nM or 2 µM. Cells were nucleofected using a 4D Nucleofector X Unit, and a GFP-positive control was included to ensure that the nucleofection worked properly. Once nucleofected, the cells were allowed to recover for 10 min at room temperature before being added to six-well plates containing warm medium. The cells were allowed to expand for several days, and a cell lysate was collected to ensure the endogenous editing worked by immunoblotting. Then, single cells were partitioned into 96-well plates to obtain isogenic clones, which were validated by immunoblotting once expanded to ensure successful HA knock-in.

Immunoprecipitation

Cells stably expressing the indicated epitope-tagged protein were cultured in 10- or 15-cm plates and allowed to reach 90% confluency before lysis. Alternatively, cells in 10-cm dishes were transiently transfected with 3 µg of the indicated plasmid DNA using Polyjet when 50% confluent. The medium was changed 1 day after transfection, and the cells were lysed 2 days after transfection with or without any necessary perturbations such as proteasomal inhibition. For lysis, cells were rinsed once with ice-cold PBS by pouring and collected by scraping in 0.7 ml (10 cm plate) or 1 ml (15 cm plate) of lysis buffer containing 0.5% CHAPS, 40 mM HEPES, pH 7.4, 100 mM NaCl, and 4 mM EDTA supplemented with 1× protease and a phosphatase inhibitor cocktail (Thermo Fisher Scientific, 78441). Cell lysates were incubated with end-to-end rotation at 4°C for 30 min before clarification by centrifugation at 21,000g for 15 min at 4°C. Anti-FLAG (Sigma, M8823,

RRID: AB_2637089) or anti-HA (Thermo Fisher Scientific, 88836, RRID: AB_2749815) magnetic beads were rinsed three times in lysis buffer using 15 μ l of beads for every harvested plate. A 50- μ l aliquot of the cell lysate was collected as input, and the remaining supernatant was incubated with the beads for 2 hours at 4°C with end-to-end rotation. The immunoprecipitants were washed three times with the same lysis buffer, and the cell lysates and immunoprecipitants were resuspended in Tris-glycine SDS sample buffer (Thermo Fisher Scientific, LC2676) containing 10% 2-mercaptoethanol. Protein was eluted by heating at 95°C for 4 min before analysis of protein content by immunoblotting.

Immunoblotting

For immunoprecipitation experiments, the collected samples were loaded directly for immunoblotting. For measuring steady-state abundance changes, cultured cells were lysed using 1 \times RIPA buffer (Boston BioProducts, BP-115X) supplemented with 1 \times protease and a phosphatase inhibitor cocktail (Thermo Fisher Scientific, 78441) for 15 min at 4°C. Samples were centrifuged at 21,000g for 15 min at 4°C, and the protein concentration was normalized using a bicinchoninic acid assay (Thermo Fisher Scientific, 23225). Clarified supernatants were resuspended in Tris-glycine SDS sample buffer (Thermo Fisher Scientific, LC2676) containing 10% 2-mercaptoethanol. Samples were loaded into 4 to 12% Tris-glycine 15-well precast gels (Thermo Fisher Scientific, XP04125BOX), and electrophoresis was run in 1 \times Tris-glycine SDS running buffer (Thermo Fisher Scientific, LC2675-4) at a constant 165 to 180 volts until the molecular weight ladder (Thermo Fisher Scientific, 26619) ran to the bottom. The protein within the gel was transferred to a 0.2- μ m nitrocellulose membrane (Bio-Rad, 170-4158) using the Trans-Blot Turbo Transfer System (Bio-Rad). Nitrocellulose membranes were then blocked using 5% milk (LabScientific, M-0842) diluted in 1 \times Tris-buffered saline plus Tween 20 (TBST) (CST, 9997S) for at least 30 min at room temperature with gentle rocking. Primary antibodies were then diluted directly in the blocking solution at a 1:1000 dilution and incubated overnight at 4°C with gentle rocking. The following primary antibodies were used: rabbit anti-EGR1 (CST, 4153, RRID: AB_2097038), rabbit anti-FosB (CST, 2251, RRID: AB_2106903), rabbit anti-c-Fos (in house) (65), rabbit anti-NR4A1 (in house, warning has high background), rabbit anti-Midnolin (Proteintech, 18939-1-AP, RRID: AB_2878569), rabbit anti-PSMD2 (CST, 25430, RRID: AB_2798903), rabbit anti-PSMA2 (CST, 2455, RRID: AB_2171400), rabbit anti-HA (CST, 3724, RRID: AB_1549585), rabbit anti-FLAG (CST, 14793, RRID: AB_2572291), rabbit anti-mTOR (CST, 2983, RRID: AB_2105622), rabbit anti-Actin (CST, 4970, RRID: AB_2223172), rabbit anti-GAPDH (CST, 5174, RRID: AB_10622025), rabbit anti-CBX4 (CST, 30559, RRID: AB_2798991),

rabbit anti-CBX8 (CST, 14696, RRID: AB_2687589), rabbit anti-ATP2 (CST, 35031, RRID: AB_2799069), rabbit anti-ATP3 (CST, 33593, RRID: AB_2799039), rabbit anti-IRF1 (CST, 8478, RRID: AB_10949108), rabbit anti-RelB (CST, 4922, RRID: AB_2179173), rabbit anti-STAT3 (CST, 9139, RRID: AB_331757), rabbit anti-SPINDOC (Sigma, HPA040128, RRID: AB_10673027), rabbit anti-XRCC1 (CST, 2735, RRID: AB_2218471), rabbit anti-CITED1 (Proteintech, 26999-1-AP, RRID: AB_2880718), rabbit anti-SOX12 (Proteintech, 23939-1-AP, RRID: AB_2879368), rabbit anti-FOXP3 (CST, 5298, RRID: AB_10839127), rabbit anti-c-Myc (CST, 5605, RRID: AB_1903938), rabbit anti-p27 (CST, 3686, RRID: AB_2077850), rabbit anti-Ubiquitin (CST, 43124, RRID: AB_2799235), and rabbit anti-IRF4 (CST, 4299, RRID: AB_10547141).

After overnight incubation, the blots were rinsed four times quickly and three additional times for longer, 10-min incubations using 1 \times TBST. After rinsing, the blots were incubated with 5% milk in 1 \times TBST and the following secondary antibodies were applied directly at a 1:2000 dilution: anti-rabbit IgG, HRP-linked (CST, 7074, RRID: AB_2099233) or anti-mouse IgG, HRP-linked (CST, 7076, RRID: AB_330924). The blots were incubated in secondary antibody for 1 hour at room temperature with gentle rocking before rinsing as done for the primary antibody. The blots were exposed to either Pierce ECL Western blotting substrate (Thermo Fisher Scientific, 32106) for strong antibodies or highly abundant protein, or Immobilon western chemiluminescent HRP substrate (Sigma, WBKLS0500) for weaker antibodies or less abundant proteins. All immunoblotting data were collected using high-sensitivity autoradiography film (Denville Scientific, E3218).

We note that the midnolin antibody (Proteintech, 18939-1-AP) has limitations that are important for readers to consider. The protein levels of endogenous midnolin appear quite low in most cell types, and this antibody contains too much background (nonspecific bands) to robustly detect endogenous midnolin protein from cell lysates at steady state. However, endogenous midnolin protein can be detected with this antibody if the cells are pretreated for a few hours with 10 μ M MG132 or if the cells are overexpressing midnolin (fig. S11B).

Mass spectrometry of endogenous midnolin immunoprecipitants

HEK-293T cells expressing endogenous 3xHA-tagged midnolin were cultured to 90% confluency in five 15-cm plates per condition, and unedited wild-type HEK-293T cells were cultured in five 15-cm plates. The knock-in cells were treated with DMSO or 10 μ M MG132 for 6 hours, with the unedited wild-type HEK-293T serving as the background, and treated with 10 μ M MG132 for 6 hours. An anti-HA immunoprecipitation was performed using the same lysis conditions and protocol as described

in the immunoprecipitation section. After the final wash, the beads were resuspended in 100 μ l of 50 mM Tris, pH 8.5, containing 5% SDS, and the samples were heated at 95°C for 5 min to elute the proteins.

Eluted proteins were then digested using trypsin on S-Trap Micro columns (Protifi, C02-micro-10) following the manufacturer's protocol. Specifically, proteins were first reduced using 5 mM Tris(2-carboxyethyl)phosphine for 15 min at 55°C, and then alkylated with 20 mM iodoacetamide for 30 min in the dark at room temperature. After alkylation, the samples were acidified using phosphoric acid to a final concentration of 2.5% (v/v) and 10 volumes of 100 mM Tris, pH 7.55 in 90% methanol/10% water were added to the samples to dilute the protein. This solution was then passed through S-Trap column by centrifugation for 30 s at 4000g. Multiple rounds of centrifugation were needed to load the entirety of one sample onto one column. Once the protein was trapped, the column was rinsed three times using 100 mM Tris, pH 7.55, in 90% methanol and 10% water, followed by a dry spin, before adding 2 μ g of trypsin suspended in 20 μ l of 50 mM ammonium bicarbonate, pH 8. Columns were kept overnight at 37°C in a humid environment. After digestion, the peptides on the column were eluted by centrifuging three times for 1 min at 4000g using three buffers applied sequentially: (i) 40 μ l of ammonium bicarbonate, pH 8; (ii) 40 μ l of 0.2% formic acid in water; and (iii) 40 μ l of 50% acetonitrile in water. The pooled peptides were dried under reduced pressure using a SpeedVac and resuspended in 30 μ l of 0.1% formic acid in water. Liquid chromatography-tandem mass spectrometry data were acquired as reported previously (66) by injecting 10 μ l of resuspended peptide sample.

A protein database consisting of the Human UniProt SwissProt proteome (downloaded on 13 November 2022) was used to identify proteins that coimmunoprecipitated with endogenous 3xHA-midnolin. Specifically, the FragPipe graphical user interface (v18.0) was used to search the data using the MSFragger search engine and to perform postprocessing of the search results. The following parameters were used in the search. Tryptic peptides with a maximum of two missed cleavages were considered. Additionally, carbamidomethylation of cysteine was set as a fixed modification, and oxidation of methionine was allowed as a variable modification, with a maximum of four variable modifications per peptide. The allowed mass tolerances were 10 ppm for precursor ions and 0.04 Da for product ions. Peptide hits were filtered to a false discovery rate of 1% using PeptideProphet as implemented in FragPipe.

Immunofluorescence

For experiments in fig. S5, A and B, 400,000 HEK-293T cells with indicated genetic background

were plated on poly-D-lysine-coated coverslips (Ted Pella, Inc.). On the following day, indicated treatments with DMSO, MG132, or PMA were performed for 6 hours before collection. Culture medium was aspirated and cells were washed with PBS once before fixation by 4% paraformaldehyde in PBS for 15 min at room temperature. After three PBS washes, cells were permeabilized with 0.05% Triton X-100 in PBS for 5 min at room temperature. Cells were washed with PBS three times and placed in immunofluorescence blocking buffer (LI-COR, 927-70001) for 45 min at room temperature. Primary antibodies mouse anti-FLAG (Sigma, F1804, RRID: AB_262044) and rabbit anti-HA (CST, 3724, RRID: AB_1549585) were diluted 1:400 in the blocking buffer and added on top of coverslips with cells for an overnight incubation at 4°C. After being rinsed three times with PBS, the cells were incubated in the dark at room temperature with secondary antibodies (1:500 dilution) and 8 μM Hoechst 33342 dye (Thermo Fisher Scientific, H3570), both diluted in blocking buffer, for 1 hour. Coverslips were rinsed thoroughly using PBS and mounted on glass slides using ProLong gold antifade mountant (Thermo Fisher Scientific, P10144).

An Alexa Fluor 488-conjugated secondary antibody was used for the FLAG (Thermo Fisher Scientific, A-11001, RRID: AB_2534069) and HA (Thermo Fisher Scientific, A-11008, RRID: AB_143165) staining in fig. S5, A and B, and the excitation wavelength was 488 nm. The excitation wavelength of the Hoechst nucleus-staining dye was 405 nm.

Image acquisition was done by a Zeiss AxioVert200M microscope with a 100× oil-immersion objective, a Yokogawa CSU-22 spinning-disk confocal head with a Borealis modification (Spectral Applied Research/Andor), and a Hamamatsu ORCA-ER CCD camera. Image acquisition and hardware were controlled by the MetaMorph software package (Molecular Devices). The excitation lasers used to capture the images were 405 and 488 nm.

RNA extraction and quantitative PCR

Total RNA was extracted from cells with the RNeasy Plus Mini Kit (Qiagen, 74134), and cDNA was generated from freshly extracted RNA using the iScript cDNA Synthesis Kit (Bio-Rad, 1708891) following the manufacturer instructions for both kits. Specifically, 250 ng of RNA was used for a 20 μl reaction to generate the cDNA. Platinum SYBR Green quantitative PCR (qPCR) Supermix-UDG (Thermo Fisher Scientific, 11733038) and 2 μl of cDNA was used for qPCR reactions. Specifically, master mixes were prepared to contain 10 μl of SYBR, 7.5 μl of water, and 0.5 μl of 40× primers per 20 μl of qPCR reaction. Quantstudio 6 Pro (Thermo Fisher Scientific) was used to run the qPCR reactions. The following intercalating premixed qPCR primers were obtained from IDT. Mouse

MIDN (Mm.PT.58.10544931): GCGTCAACTTGCTCCCAT, AACGCCTCAAGTACCCAAG; mouse EGRI (Mm.PT.58.29064929): GATAACTCGTCTCCACCATCG, AGCGCCTTCAATCCTCAAG; mouse c-Fos (Mm.PT.58.29977214): GGCACTAGAGACGGACAGAT, ACAGCCTTCTCTACTACCATTG; mouse FosB (Mm.PT.58.10990878): AGAGACACCTTACCCAGAAGA, GCTCTGCCTTTCTCTCTCA; mouse Actin (Mm.PT.39a.22214843.g): GACTCATCTGACTCTCTGCTTG, GATTACTGCTCTGGCTCCTAG; mouse mTOR (Mm.PT.58.28403918): TGCATCACTCGTTCATCCTG, AAGTCATCACATCCAAGCAGA.

Changes in mRNA levels were determined by subtracting the cycle quantification (Cq) values generated during the qPCR between the gene of interest and the control to yield a ΔCq value. Data were then normalized to the indicated control condition by subtracting the ΔCq values by the average ΔCq of the indicated control condition to generate the ΔΔCq. Plotted in graphs are $2^{-\Delta\Delta Cq}$ from three biological replicates and the following statistical tests were used.

For Fig. 2, E and F, data were analyzed using an ordinary one-way ANOVA followed by a Tukey's multiple-comparisons test where $****P < 0.0001$. For fig. S1D, data were analyzed using a two-way ANOVA followed by Šidák's multiple comparisons test, where ns is not significant and $***P < 0.001$.

Computational identification of substrate β strands AlphaFold multimer predictions

To identify β strands within hits identified in the ORFeome GPS screen, genes with ΔPSI < -0.5 were taken ($n = 508$) and the longest sequence across corresponding protein accession IDs (either NCBI Reference Sequence or Ensembl ID) was used as the input sequence for downstream steps (because barcodes from the screen were grouped at the gene level but could represent multiple isoforms). These sequences were individually paired with the MIDN sequence (UniProtKB: Q504T8) as a two-sequence FASTA file input into AlphaFold (v2.2.0) for multimer prediction with default reference databases specified as in (26) and max_template_date=2022-01-01. Any selenocysteines were recoded as cysteines, and three substrates (ACSBG2, ACSS2, and RIMBP3) that failed MSA using the default settings were rerun successfully by replacing the UniClust30_2018_08 database with UniRef30_2022_02.

Identification of substrate β strands within midnolin β sheet

The 25 ranked PDB models from each AlphaFold run with MIDN and one of the substrates were then processed by a custom Python script to identify PDB models that folded a linear stretch of the substrate into β-strand conformation placed between β strands of the corresponding MIDN domain. In more detail, a pairwise dis-

tance matrix was first computed between each α-carbon atom in MIDN and each α-carbon atom in the substrate as

$$D_{i,j} = \sqrt{(x_i - x_j)^2 + (y_i - y_j)^2 + (z_i - z_j)^2}$$

where x_i , y_i , and z_i are the coordinates of the i^{th} substrate α-carbon atom and x_j , y_j , and z_j are the coordinates of the j^{th} MIDN α-carbon atom. Because most β sheets have interstrand distances <5 Å (67), the distance matrix was scanned to identify sequential substrate residues <5.5 Å from corresponding linear stretches within each adjacent MIDN β strand (ie. $D_{i,j} < 5.5$ for both some sequential set of i with some sequential set of j , where $148 \leq j \leq 157$, as well as the same set of i with another sequential set of j , where $279 \leq j \leq 286$).

Secondary structure assignment for the PDB model was done with the DSSP algorithm (68). Substrate residues satisfying the distance requirements specified above were then retained if they were assigned the extended β strand secondary structure (i.e., “E” coding). Because DSSP relies on flanking residues to call secondary structure, the most N- and C-terminal residues are not assigned secondary structure. To avoid excluding them from β-strand assignments, they were assigned “E” coding if the adjacent residue had been assigned “E” coding. To catch residues that are part of a β strand but slightly further from one or both of the MIDN β strands, this set of residues was then expanded by seven residues in each direction, and, again, only those with an extended β-strand secondary structure were kept. Finally, the longest contiguous stretch of β-strand secondary structure was kept (if any) for final reporting (data S4).

Properties of identified substrate β strands Relative disorder comparison

ORFs used in AlphaFold multimer folding alongside midnolin were matched with UniProtKB accessions using UniParc to find identical proteins that had already been folded as monomers in the AlphaFold Protein Structure Database (<https://alphafold.ebi.ac.uk/>). This yielded existing models for 126 of 205 substrates predicted to interact with the midnolin Catch domain, for which the predicted local distance difference test (pLDDT) scores were extracted from corresponding PDB files. The pLDDT scores for these residues interacting with the midnolin Catch domain were averaged and compared with the average of the rest of the substrate (paired t test, $P = 2.72 \times 10^{-9}$) as an approximation of disorder in the original substrate (69), where lower pLDDT scores correspond to increased disorder. The regions that are predicted to interact with the Catch domain are predicted to be unstructured by AlphaFold in the native, midnolin-free state.

Amino acid enrichment

For each residue, n , going into the β strand from either the N- or C-terminal side, the overall frequency of each amino acid for β strands of length $\geq 2n$ (to avoid double counting) was normalized by the background amino acid frequency across substrate sequences. Frequencies were then computed for amino acids before and after all β strands provided the β strand was not the N or C terminus of the protein, respectively.

Hydrophobicity

The relative hydrophobicity of residues comprising the MIDN-interacting β strand was assessed by a two-sided paired t test between the mean hydrophobicity index (70, 71) (at pH 7) of residues in the β strand with that of residues comprising the rest of the substrate.

Identification of MIDN-facing β -strand side chains

Because β strands within a β sheet make contacts with each other through backbone interactions, where side chains alternately project above and below the plane of the β sheet, residues composing the MIDN-interacting β strand can be parsed into those facing toward or away from the MIDN Catch domain. Side chains of the substrate β strand facing the MIDN Catch domain were identified by first generating another distance matrix as before, but between each α -carbon atom in MIDN and each β -carbon atom in the substrate. For each residue in the identified substrate β strand, those with β -carbon distance to MIDN Catch domain (approximated by α -carbon position for MIDN isoleucine residue 309) less than their α -carbon distance were annotated as MIDN-facing. Because glycine lacks a β -carbon and residues at the ends of β strands may have more rotational variability, but side chain orientations along the β strand should alternate between facing toward or away from the MIDN Catch domain, a filter was then applied to determine whether the identified MIDN-facing side chains better matched either the set of odd or set of even residues. MIDN-facing side chains were then annotated as that set. Properties such as relative frequency and hydrophobicity were then computed for inward- and outward-facing side chains.

REFERENCES AND NOTES

1. K. Minatohara, M. Akiyoshi, H. Okuno, Role of immediate-early genes in synaptic plasticity and neuronal ensembles underlying the memory trace. *Front. Mol. Neurosci.* **8**, 78 (2016). PMID: 26778955
2. S. B. McMahon, J. G. Monroe, The role of early growth response gene 1 (*egr-1*) in regulation of the immune response. *J. Leukoc. Biol.* **60**, 159–166 (1996). doi: 10.1002/jlb.60.2.159; PMID: 8773576
3. E. L. Yap, M. E. Greenberg, Activity-regulated transcription: Bridging the gap between neural activity and behavior. *Neuron* **100**, 330–348 (2018). doi: 10.1016/j.neuron.2018.10.013; PMID: 30359600
4. E. Benito, A. Barco, The neuronal activity-driven transcriptome. *Mol. Neurobiol.* **51**, 1071–1088 (2015). doi: 10.1007/s12035-014-8772-z; PMID: 24935719
5. S. Bahrami, F. Drabløs, Gene regulation in the immediate-early response process. *Adv. Biol. Regul.* **62**, 37–49 (2016). doi: 10.1016/j.jbior.2016.05.001; PMID: 27220739
6. G. Bossis, P. Ferrara, C. Acquaviva, I. Jariel-Encontre, M. Piechaczyk, c-Fos proto-oncogene is degraded by the proteasome independently of its own ubiquitinylation in vivo. *Mol. Cell. Biol.* **23**, 7425–7436 (2003). doi: 10.1128/MCB.23.20.7425-7436.2003; PMID: 14517309
7. T. Gomard *et al.*, Fos family protein degradation by the proteasome. *Biochem. Soc. Trans.* **36**, 858–863 (2008). doi: 10.1042/BST0360858; PMID: 18793151
8. H. C. Yen, Q. Xu, D. M. Chou, Z. Zhao, S. J. Elledge, Global protein stability profiling in mammalian cells. *Science* **322**, 918–923 (2008). doi: 10.1126/science.1160489; PMID: 18988847
9. M. E. Greenberg, E. B. Ziff, Stimulation of 3T3 cells induces transcription of the c-fos proto-oncogene. *Nature* **311**, 433–438 (1984). doi: 10.1038/311433a0; PMID: 6090941
10. J. Y. Joo, K. Schaukowitz, L. Farbiak, G. Kilaru, T. K. Kim, Stimulus-specific combinatorial functionality of neuronal c-fos enhancers. *Nat. Neurosci.* **19**, 75–83 (2016). doi: 10.1038/nn.4170; PMID: 26559656
11. A. R. Mardinly *et al.*, Sensory experience regulates cortical inhibition by inducing IGF1 in VIP neurons. *Nature* **531**, 371–375 (2016). doi: 10.1038/nature17187; PMID: 26958833
12. N. Sagehashi *et al.*, Insulin enhances gene expression of midnolin, a novel genetic risk factor for Parkinson's disease, via extracellular signal-regulated kinase, phosphoinositide 3-kinase and multiple transcription factors in SH-SY5Y cells. *J. Pharmacol. Exp. Ther.* **381**, 68–78 (2022). doi: 10.1124/jpet.121.001076; PMID: 35241633
13. I. Koren *et al.*, The eukaryotic proteome is shaped by E3 ubiquitin ligases targeting C-terminal degrons. *Cell* **173**, 1622–1635.e14 (2018). doi: 10.1016/j.cell.2018.04.028; PMID: 29779948
14. J. Du *et al.*, Stuxnet facilitates the degradation of polycomb protein during development. *Dev. Cell* **37**, 507–519 (2016). doi: 10.1016/j.devcel.2016.05.013; PMID: 27326929
15. H. W. Mittrücker *et al.*, Requirement for the transcription factor LSRIF/IRF4 for mature B and T lymphocyte function. *Science* **275**, 540–543 (1997). doi: 10.1126/science.275.5299.540; PMID: 8999800
16. U. Klein *et al.*, Transcription factor IRF4 controls plasma cell differentiation and class-switch recombination. *Nat. Immunol.* **7**, 773–782 (2006). doi: 10.1038/ni1357; PMID: 16767092
17. E. L. Huttlin *et al.*, Dual proteome-scale networks reveal cell-specific remodeling of the human interactome. *Cell* **184**, 3022–3040.e28 (2021). doi: 10.1016/j.cell.2021.04.011; PMID: 33961781
18. T. H. Wu, L. Shi, A. W. Lowe, M. R. Nicolls, P. N. Kao, Inducible expression of immediate early genes is regulated through dynamic chromatin association by NF45/ILF2 and NF90/NF110/ILF3. *PLoS ONE* **14**, e0216042 (2019). doi: 10.1371/journal.pone.0216042; PMID: 31022259
19. M. L. Hyer *et al.*, A small-molecule inhibitor of the ubiquitin activating enzyme for cancer treatment. *Nat. Med.* **24**, 186–193 (2018). doi: 10.1038/nm.4474; PMID: 29334375
20. A. Montagnoli *et al.*, Ubiquitination of p27 is regulated by Cdk-dependent phosphorylation and trimeric complex formation. *Genes Dev.* **13**, 1181–1189 (1999). doi: 10.1101/gad.13.9.1181; PMID: 10323868
21. L. M. Tsvetkov, K. H. Yeh, S. J. Lee, H. Sun, H. Zhang, p27(Kip1) ubiquitination and degradation is regulated by the SCF(Skp2) complex through phosphorylated Thr187 in p27. *Curr. Biol.* **9**, 661–664 (1999). doi: 10.1016/S0960-9822(99)80290-5; PMID: 10375532
22. M. Welcker *et al.*, Two diphosphorylated degrons control c-Myc degradation by the Fbw7 tumor suppressor. *Sci. Adv.* **8**, eabi7872 (2022). doi: 10.1126/sciadv.abi7872; PMID: 35089787
23. M. M. Peña, Y. Y. Xing, S. Koli, F. G. Berger, Role of N-terminal residues in the ubiquitin-independent degradation of human thymidylate synthase. *Biochem. J.* **394**, 355–363 (2006). doi: 10.1042/BJ20051479; PMID: 16259621
24. K. N. Swatek, D. Komander, Ubiquitin modifications. *Cell Res.* **26**, 399–422 (2016). doi: 10.1038/cr.2016.39; PMID: 27012465
25. V. Chau *et al.*, A multiubiquitin chain is confined to specific lysine in a targeted short-lived protein. *Science* **243**, 1576–1583 (1989). doi: 10.1126/science.2538923; PMID: 2538923
26. J. Jumper *et al.*, Highly accurate protein structure prediction with AlphaFold. *Nature* **596**, 583–589 (2021). doi: 10.1038/s41586-021-03819-2; PMID: 34265844
27. N. Zheng, N. Shabek, Ubiquitin ligases: Structure, function, and regulation. *Annu. Rev. Biochem.* **86**, 129–157 (2017). doi: 10.1146/annurev-biochem-060815-014922; PMID: 28375744
28. I. Dikic, S. Wakatsuki, K. J. Walters, Ubiquitin-binding domains - from structures to functions. *Nat. Rev. Mol. Cell Biol.* **10**, 659–671 (2009). doi: 10.1038/nrm2767; PMID: 19737779
29. C. Schaubert *et al.*, Rad23 links DNA repair to the ubiquitin/proteasome pathway. *Nature* **391**, 715–718 (1998). doi: 10.1038/35661; PMID: 9490418
30. S. Elsassser *et al.*, Proteasome subunit Rpn1 binds ubiquitin-like protein domains. *Nat. Cell Biol.* **4**, 725–730 (2002). doi: 10.1038/ncb845; PMID: 12198495
31. A. Bachmair, D. Finley, A. Varshavsky, In vivo half-life of a protein is a function of its amino-terminal residue. *Science* **234**, 179–186 (1986). doi: 10.1126/science.3018930; PMID: 3018930
32. A. Varshavsky, Naming a targeting signal. *Cell* **64**, 13–15 (1991). doi: 10.1016/0092-8674(91)90202-A; PMID: 1986863
33. R. T. Timms, I. Koren, Tying up loose ends: The N-degron and C-degron pathways of protein degradation. *Biochem. Soc. Trans.* **48**, 1557–1567 (2020). doi: 10.1042/BST20191094; PMID: 32627813
34. A. Varshavsky, N-degron and C-degron pathways of protein degradation. *Proc. Natl. Acad. Sci. U.S.A.* **116**, 358–366 (2019). doi: 10.1073/pnas.1816596116; PMID: 30622213
35. E. J. Nestler, M. Barrot, D. W. Self, DeltaFosB: A sustained molecular switch for addiction. *Proc. Natl. Acad. Sci. U.S.A.* **98**, 11042–11046 (2001). doi: 10.1073/pnas.191352698; PMID: 11572966
36. B. T. Hope *et al.*, Induction of a long-lasting AP-1 complex composed of altered Fos-like proteins in brain by chronic cocaine and other chronic treatments. *Neuron* **13**, 1235–1244 (1994). doi: 10.1016/0896-6273(94)90061-2; PMID: 7946359
37. M. B. Kelz *et al.*, Expression of the transcription factor deltaFosB in the brain controls sensitivity to cocaine. *Nature* **401**, 272–276 (1999). doi: 10.1038/45790; PMID: 10499584
38. S. C. Li, N. K. Goto, K. A. Williams, C. M. Deber, Alpha-helical, but not beta-sheet, propensity of proline is determined by peptide environment. *Proc. Natl. Acad. Sci. U.S.A.* **93**, 6676–6681 (1996). doi: 10.1073/pnas.93.13.6676; PMID: 8692877
39. M. Tsukahara, H. Suemori, S. Noguchi, Z. S. Ji, H. Tsunoo, Novel nuclear protein, midnolin, is expressed in the mesencephalon during mouse development. *Gene* **254**, 45–55 (2000). doi: 10.1016/S0378-1119(00)00259-6; PMID: 10974535
40. F. T. Gallo, C. Katche, J. F. Morici, J. H. Medina, N. V. Weisstaub, Immediate early genes, memory and psychiatric disorders: Focus on c-Fos, Egr1 and Arc. *Front. Behav. Neurosci.* **12**, 79 (2018). doi: 10.3389/fnbeh.2018.00079; PMID: 29755331
41. A. L. Shaffer *et al.*, IRF4 addiction in multiple myeloma. *Nature* **454**, 226–231 (2008). doi: 10.1038/nature07064; PMID: 18568025
42. P. S. Biswas, G. Bhagat, A. B. Pernis, IRF4 and its regulators: Evolving insights into the pathogenesis of inflammatory arthritis? *Immunol. Rev.* **233**, 79–96 (2010). doi: 10.1111/j.0105-2896.2009.00864.x; PMID: 20192994
43. R. Nayar *et al.*, TCR signaling via Tec kinase ITK and interferon regulatory factor 4 (IRF4) regulates CD8+ T-cell differentiation. *Proc. Natl. Acad. Sci. U.S.A.* **109**, E2794–E2802 (2012). doi: 10.1073/pnas.1205742109; PMID: 23011795
44. J. W. Williams *et al.*, Transcription factor IRF4 drives dendritic cells to promote Th2 differentiation. *Nat. Commun.* **4**, 2990 (2013). doi: 10.1038/ncomms3990; PMID: 24356538
45. J. Eguchi *et al.*, Transcriptional control of adipose lipid handling by IRF4. *Cell Metab.* **13**, 249–259 (2011). doi: 10.1016/j.cmet.2011.02.005; PMID: 21356515
46. Y. Murakami, S. Matsufuji, S. Hayashi, N. Tanahashi, K. Tanaka, Degradation of ornithine decarboxylase by the 26S proteasome. *Biochem. Biophys. Res. Commun.* **267**, 1–6 (2000). doi: 10.1006/bbrc.1999.1706; PMID: 10623564
47. L. Ghoda, T. van Daalen Wetters, M. Macrae, D. Ascherman, P. Coffino, Prevention of rapid intracellular degradation of ODC by a carboxyl-terminal truncation. *Science* **243**, 1493–1495 (1989). doi: 10.1126/science.2928784; PMID: 2928784
48. Y. Murakami *et al.*, Ornithine decarboxylase is degraded by the 26S proteasome without ubiquitination. *Nature* **360**, 597–599 (1992). doi: 10.1038/360597a0; PMID: 1334232
49. M. A. Hoyt, M. Zhang, P. Coffino, Ubiquitin-independent mechanisms of mouse ornithine decarboxylase degradation are conserved between mammalian and fungal cells. *J. Biol. Chem.* **278**, 12135–12143 (2003). doi: 10.1074/jbc.M211802200; PMID: 12562772
50. J. S. Merkel, J. M. Sturtevant, L. Regan, Sidechain interactions in parallel beta sheets: The energetics of cross-strand pairings. *Structure* **7**, 1333–1343 (1999). doi: 10.1016/S0969-2126(00)80023-4; PMID: 10574793
51. I. Marín, The ubiquitin gene family: Evolutionary patterns and functional insights. *BMC Evol. Biol.* **14**, 63 (2014). doi: 10.1186/1471-2148-14-63; PMID: 24674348

52. S. Raasi, C. M. Pickart, Rad23 ubiquitin-associated domains (UBA) inhibit 26 S proteasome-catalyzed proteolysis by sequestering lysine 48-linked polyubiquitin chains. *J. Biol. Chem.* **278**, 8951–8959 (2003). doi: [10.1074/jbc.M212841200](https://doi.org/10.1074/jbc.M212841200); pmid: [12643283](https://pubmed.ncbi.nlm.nih.gov/12643283/)
53. L. Chen, U. Shinde, T. G. Orlton, K. Madura, Ubiquitin-associated (UBA) domains in Rad23 bind ubiquitin and promote inhibition of multi-ubiquitin chain assembly. *EMBO Rep.* **2**, 933–938 (2001). doi: [10.1093/embo-reports/kve203](https://doi.org/10.1093/embo-reports/kve203); pmid: [11571271](https://pubmed.ncbi.nlm.nih.gov/11571271/)
54. K. K. Joshi, M. Bergé, S. K. Radhakrishnan, P. H. Viollier, P. Chien, An adaptor hierarchy regulates proteolysis during a bacterial cell cycle. *Cell* **163**, 419–431 (2015). doi: [10.1016/j.cell.2015.09.030](https://doi.org/10.1016/j.cell.2015.09.030); pmid: [26451486](https://pubmed.ncbi.nlm.nih.gov/26451486/)
55. N. J. Kuhlmann, D. Dosey, P. Chien, Cargo competition for a dimerization interface restricts and stabilizes a bacterial protease adaptor. *Proc. Natl. Acad. Sci. U.S.A.* **118**, e2010523118 (2021). doi: [10.1073/pnas.2010523118](https://doi.org/10.1073/pnas.2010523118); pmid: [33875581](https://pubmed.ncbi.nlm.nih.gov/33875581/)
56. N. Sharma et al., ARNT2 tunes activity-dependent gene expression through NCoR2-mediated repression and NPAS4-mediated activation. *Neuron* **102**, 390–406.e9 (2019). doi: [10.1016/j.neuron.2019.02.007](https://doi.org/10.1016/j.neuron.2019.02.007); pmid: [30846309](https://pubmed.ncbi.nlm.nih.gov/30846309/)
57. J. G. Doench et al., Optimized sgRNA design to maximize activity and minimize off-target effects of CRISPR-Cas9. *Nat. Biotechnol.* **34**, 184–191 (2016). doi: [10.1038/nbt.3437](https://doi.org/10.1038/nbt.3437); pmid: [26780180](https://pubmed.ncbi.nlm.nih.gov/26780180/)
58. R. T. Timms et al., A glycine-specific N-degron pathway mediates the quality control of protein N-myristoylation. *Science* **365**, eaaw4912 (2019). doi: [10.1126/science.aaw4912](https://doi.org/10.1126/science.aaw4912); pmid: [31273098](https://pubmed.ncbi.nlm.nih.gov/31273098/)
59. T. D. Martin et al., The adaptive immune system is a major driver of selection for tumor suppressor gene inactivation. *Science* **373**, 1327–1335 (2021). doi: [10.1126/science.abg5784](https://doi.org/10.1126/science.abg5784); pmid: [34529489](https://pubmed.ncbi.nlm.nih.gov/34529489/)
60. M. Martin, Cutadapt removes adapter sequences from high-throughput sequencing reads. *EMBnet. J.* **17**, 10–12 (2011). doi: [10.14806/ej.17.1.200](https://doi.org/10.14806/ej.17.1.200)
61. B. Langmead, S. L. Salzberg, Fast gapped-read alignment with Bowtie 2. *Nat. Methods* **9**, 357–359 (2012). doi: [10.1038/nmeth.1923](https://doi.org/10.1038/nmeth.1923); pmid: [22388286](https://pubmed.ncbi.nlm.nih.gov/22388286/)
62. W. Li et al., MAGeCK enables robust identification of essential genes from genome-scale CRISPR/Cas9 knockout screens. *Genome Biol.* **15**, 554 (2014). doi: [10.1186/s13059-014-0554-4](https://doi.org/10.1186/s13059-014-0554-4); pmid: [25476604](https://pubmed.ncbi.nlm.nih.gov/25476604/)
63. A. Subramanian et al., Gene set enrichment analysis: A knowledge-based approach for interpreting genome-wide expression profiles. *Proc. Natl. Acad. Sci. U.S.A.* **102**, 15545–15550 (2005). doi: [10.1073/pnas.0506580102](https://doi.org/10.1073/pnas.0506580102); pmid: [16199517](https://pubmed.ncbi.nlm.nih.gov/16199517/)
64. A. Liberzon et al., Molecular signatures database (MSigDB) 3.0. *Bioinformatics* **27**, 1739–1740 (2011). doi: [10.1093/bioinformatics/btr260](https://doi.org/10.1093/bioinformatics/btr260); pmid: [21546393](https://pubmed.ncbi.nlm.nih.gov/21546393/)
65. Y. Lin et al., Activity-dependent regulation of inhibitory synapse development by Npas4. *Nature* **455**, 1198–1204 (2008). doi: [10.1038/nature07319](https://doi.org/10.1038/nature07319); pmid: [18815592](https://pubmed.ncbi.nlm.nih.gov/18815592/)
66. C. Nardone et al., A central role for regulated protein stability in the control of TFE3 and MITF by nutrients. *Mol. Cell* **83**, 57–73.e9 (2023). doi: [10.1016/j.molcel.2022.12.013](https://doi.org/10.1016/j.molcel.2022.12.013); pmid: [36608670](https://pubmed.ncbi.nlm.nih.gov/36608670/)
67. J. Martin et al., Protein secondary structure assignment revisited: A detailed analysis of different assignment methods. *BMC Struct. Biol.* **5**, 17 (2005). doi: [10.1186/1472-6807-5-17](https://doi.org/10.1186/1472-6807-5-17); pmid: [16164759](https://pubmed.ncbi.nlm.nih.gov/16164759/)
68. W. Kabsch, C. Sander, Dictionary of protein secondary structure: Pattern recognition of hydrogen-bonded and geometrical features. *Biopolymers* **22**, 2577–2637 (1983). doi: [10.1002/bip.360221211](https://doi.org/10.1002/bip.360221211); pmid: [6667333](https://pubmed.ncbi.nlm.nih.gov/6667333/)
69. K. Tunyasuvunakool et al., Highly accurate protein structure prediction for the human proteome. *Nature* **596**, 590–596 (2021). doi: [10.1038/s41586-021-03828-1](https://doi.org/10.1038/s41586-021-03828-1); pmid: [34293799](https://pubmed.ncbi.nlm.nih.gov/34293799/)
70. O. D. Monera, T. J. Sereda, N. E. Zhou, C. M. Kay, R. S. Hodges, Relationship of sidechain hydrophobicity and alpha-helical propensity on the stability of the single-stranded amphipathic alpha-helix. *J. Pept. Sci.* **1**, 319–329 (1995). doi: [10.1002/psc.310010507](https://doi.org/10.1002/psc.310010507); pmid: [9223011](https://pubmed.ncbi.nlm.nih.gov/9223011/)
71. T. J. Sereda, C. T. Mant, F. D. Sönnichsen, R. S. Hodges, Reversed-phase chromatography of synthetic amphipathic alpha-helical peptides as a model for ligand/receptor interactions. Effect of changing hydrophobic environment on the relative hydrophilicity/hydrophobicity of amino acid side-chains. *J. Chromatogr. A* **676**, 139–153 (1994). doi: [10.1016/0021-9673\(94\)00371-8](https://doi.org/10.1016/0021-9673(94)00371-8); pmid: [7921171](https://pubmed.ncbi.nlm.nih.gov/7921171/)
72. G. A. Collins, A. L. Goldberg, Proteins containing ubiquitin-like (Ubl) domains not only bind to 26S proteasomes but also induce their activation. *Proc. Natl. Acad. Sci. U.S.A.* **117**, 4664–4674 (2020). doi: [10.1073/pnas.1915534117](https://doi.org/10.1073/pnas.1915534117); pmid: [32071216](https://pubmed.ncbi.nlm.nih.gov/32071216/)
73. X. Gu et al., Data for: The midnolin-proteasome pathway catches proteins for ubiquitination-independent degradation, Dryad (2023); <https://doi.org/10.5061/dryad.m905qfv6g>.

ACKNOWLEDGMENTS

We thank all members of the Greenberg and Elledge labs for helpful suggestions and contributions, especially T. Whitwam, O. Dagliyan, and L. Hu for the generous gift of the NR4A1 antibody and I. Vogel, E. Assad, and N. Pajarillo for help with primary cortical neuron dissection. We also thank T. Martin for help with the midnolin knock-in strategy and M. Dezfalian for sharing unpublished expression vectors; J. Nelson and the Harvard Medical School Department of Immunology Flow Cytometry Core Facility for invaluable help in cell sorting the genetic screens; the Research Computing Group at Harvard Medical School as AlphaFold analyses were performed on the O2 High Performance Compute Cluster; B. Palanski and P. Cole for access and help with mass spectrometry; and A. Goldberg, S. Shao, and M. Negasi for valuable suggestions

for our manuscript. Raw data for this manuscript can be accessed using Dryad (73). **Funding:** This work was supported by the National Institutes of Health (NIH grant R01 NS115965 to M.E.G.; and National Institute on Aging grant AG11085 to S.J.E.), X.G. is the National Mah Jongg League Fellow of the Damon Runyon Cancer Research Foundation (DRG-2469-22). C.N. is supported by the National Science Foundation Graduate Research Fellowship program. N.K. is supported by funding from the NIH (grant T32 HG002295). S.J.E. is an investigator with the Howard Hughes Medical Institute. The Greenberg Laboratory is supported by the Allen Discovery Center Program, a Paul G. Allen Frontiers Group advised program of the Paul G. Allen Family Foundation, and the Tang-Yang Autism Center at Harvard Medical School. **Author contributions:** The study was conceptualized by X.G. and C.N. Wet and dry experiments were performed by X.G., C.N., N.K., and A.M. Funding was secured by S.J.E. and M.E.G. The study was supervised by S.J.E. and M.E.G. The manuscript was written by X.G., C.N., S.J.E., and M.E.G.

Competing interests: S.J.E. is a founder of TSCAN Therapeutics, MAZE Therapeutics, ImmunelD, and Mirimus serves on the scientific advisory boards of Homology Medicines, ImmunelD, MAZE Therapeutics, X-Chem, and TSCAN Therapeutics; and is an adviser for MPM Capital. The remaining authors declare no competing interests. **Data and materials availability:** Any reagents that are unique to this study will be made available upon request. Requests for reagents or any additional information necessary to reanalyze the data reported in this paper should be directed to and will be fulfilled by the corresponding authors. The raw DNA sequencing data, mass spectrometry data, and PDB files for the midnolin-substrate AlphaFold predictions were deposited to Dryad (73). **License information:** Copyright © 2023 the authors, some rights reserved; exclusive licensee American Association for the Advancement of Science. No claim to original US government works. <https://www.science.org/about/science-licenses-journal-article-reuse> This article is subject to HHMI's Open Access to Publications policy. HHMI lab heads have previously granted a nonexclusive CC BY 4.0 license to the public and a sublicensable license to HHMI in their research articles. Pursuant to those licenses, the author-accepted manuscript (AAM) of this article can be made freely available under a CC BY 4.0 license immediately upon publication.

SUPPLEMENTARY MATERIALS

science.org/doi/10.1126/science.adh5021

Figs. S1 to S11

References

Data S1 to S4

MDAR Reproducibility Checklist

Submitted 8 March 2023; resubmitted 1 June 2023

Accepted 11 July 2023

[10.1126/science.adh5021](https://doi.org/10.1126/science.adh5021)